CORNELL UNIVERSITY
DESIGN BUILD FLY
DESIGN REPORT 2024-2025

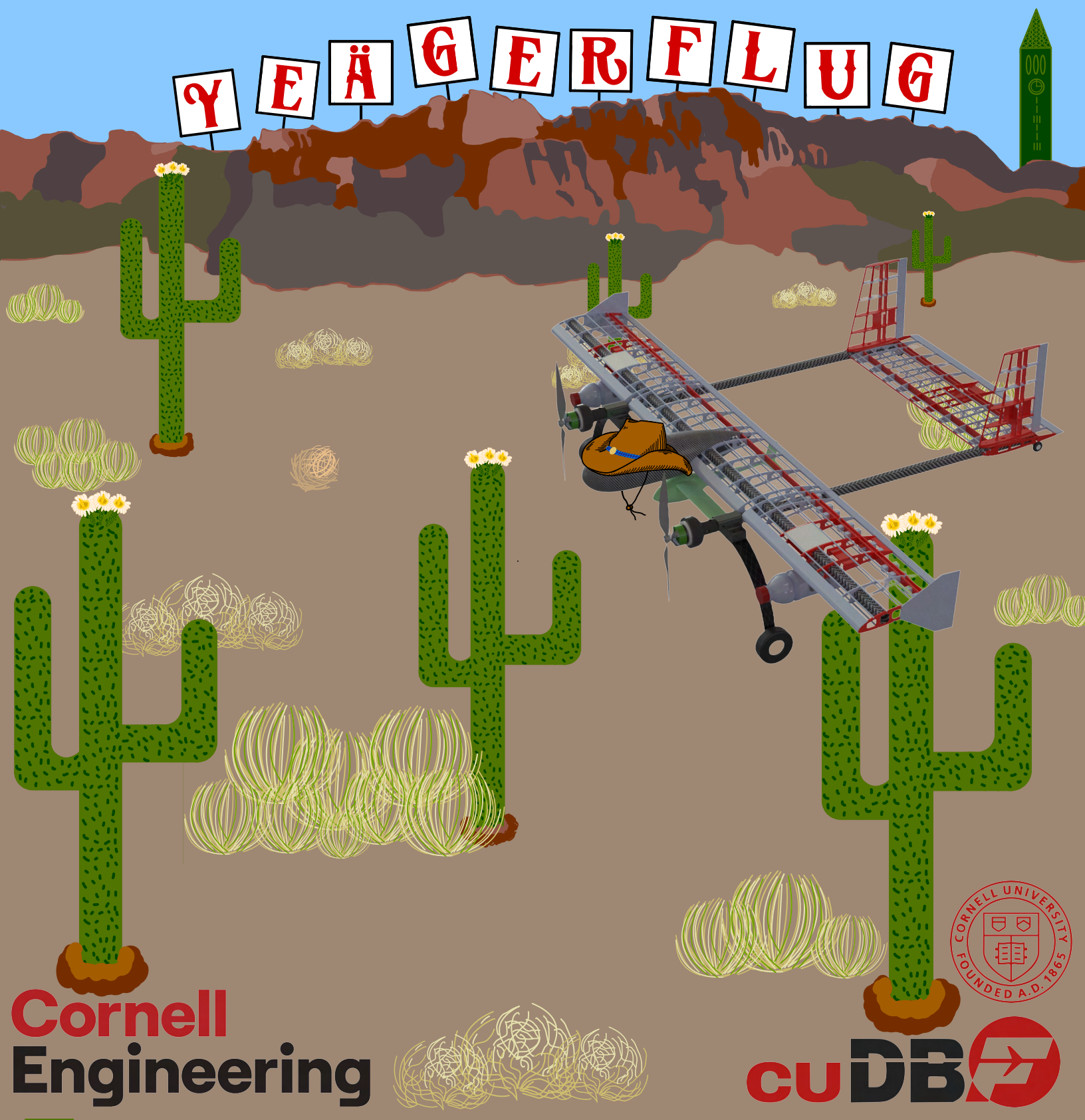

Cornell Engineering

CUDBF

Contents

1 Executive Summary

This report details the design, manufacturing, and testing processes of Cornell University Design Build Fly for the 2024-2025 American Institute of Aeronautics and Astronautics (AIAA) Design, Build, Fly (DBF) competition. The team's entry to the competition is Yeägerflug which completes an X-1 Supersonic Flight Test Program, including four missions. Mission 1 (M1) is a delivery flight without payloads, Mission 2 (M2) is a captive carry flight with loaded external payloads. Mission 3 (M3) is a launch flight with fuel tanks and an X-1 test vehicle, which is released mid-mission. The ground mission (GM) is a demonstration of the aircraft's ability to be easily converted from a bomber to an X-1 testbed.

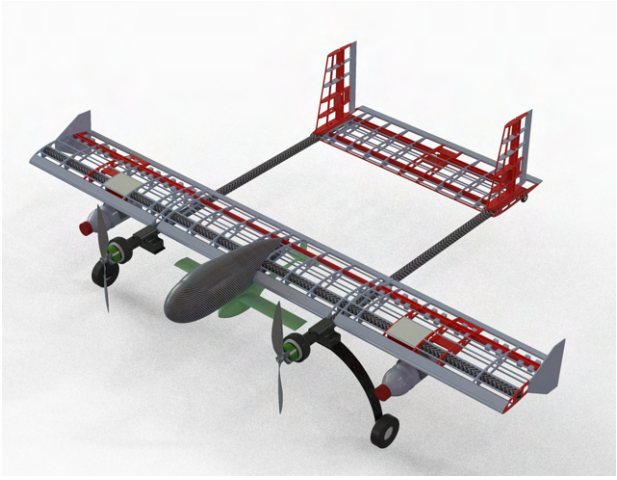

Figure 1.0.1: Yeägerflug finalized design

Yeägerflug was designed in an iterative process that included three major phases. The first phase, conceptual design, was an exploration of the design space. This included a breakdown of mission requirements and scoring sensitivity studies. The preliminary design phase sized major aircraft components including the wing, the empennage, and the electronic system based on trade studies and design optimization simulations. The final phase, detailed design, focused on the internal structure of the major subsystems and their integration with each other. This process yielded a dual motor, twin-boom aircraft, with an H-tail, a mid-wing, and a tail dragger landing gear configuration. The twin-boom design moves major structural components to the side, allowing space for the X-1 test vehicle. This vehicle is an autonomous foam glider with an ArduPilot flight computer. The dual motor and H-tail configurations take advantage of the two tail booms, increasing the structural stability of the aircraft. The tail dragger landing gear was also selected to further utilize the tail booms. Yeägerflug is constructed out of a combination of balsa, basswood, carbon fiber, and 3D-printed components. The team undertook a rigorous testing process of all systems and subsystems to ensure that the aircraft meets all competition requirements.

The remainder of this design report provides 1) an overview of the team and team structure, outlining the team organization, workflow, and timeline, 2) a discussion of the conceptual design process, including the mission requirements, a scoring sensitivity analysis, and trade studies to determine the overall configuration, 3) the preliminary design process detailing the design and analysis methodology, how sizing was conducted, and aerodynamic analysis, 4) the detailed design of Yeägerflug's subsystems, key parameters, flight performance estimates, and a CAD drawing package, and 5) a description of how manufacturing and various tests were completed, as well as results from those tests. Critical data and a rendering of the aircraft design are shown in **Table 1.0.1** and **Figure 1.0.1** respectively.

Parameter	M1	M2	M3
Mass (lbs)	7.45	12.35	8.27
Cruise Velocity (ft/s)	132.64	141.89	93.45
Flight time (min)	1.98	2.32	5.00
# of laps	3	3	7
Fuel Tank Mass (lbs)	0.00	4.18	0.44
X-1 Mass (lbs)	0.00	0.49	0.49

Table 1.0.1: Yeägerflug predicted mission parameters

2 Management Summary

2.1 Team Organization

CUDBF is a 30 person, student-led project team at Cornell University. The team is led by a chief engineer and a project manager, who are supported by the safety officer. The chief engineer guides the technical direction of the team, overseeing design decisions and ensuring that the aircraft meets all competition objectives. The project manager is responsible for team logistics, including scheduling and recruitment. The safety officer ensures team well-being by establishing workspace safety procedures and serving as a contact for team members to voice concerns. The leadership team works closely with a faculty advisor, project team staff, and model aviation experts in the surrounding community to bring diverse perspectives to the team's work.

The remainder of CUDBF is divided into four subteams as illustrated in **Figure 2.1.1**. The three technical subteams are each responsible for one of the major disciplines of aircraft design. The Aerodynamics subteam designs the flight surfaces and control surfaces, as well as conducting aerodynamic analysis of proposed aircraft designs. The Mechanical subteam develops the structure of the airframe and integrates various parts into the aircraft body. The Propulsion subteam coordinates all propulsive and electronic components. The Business subteam handles project management, including financials and community outreach. Subteam leads oversee the design process, coordinate between subteams, and keep the project on schedule. Each subteam leads' responsibilities are divided into separate categories for better organization and management.

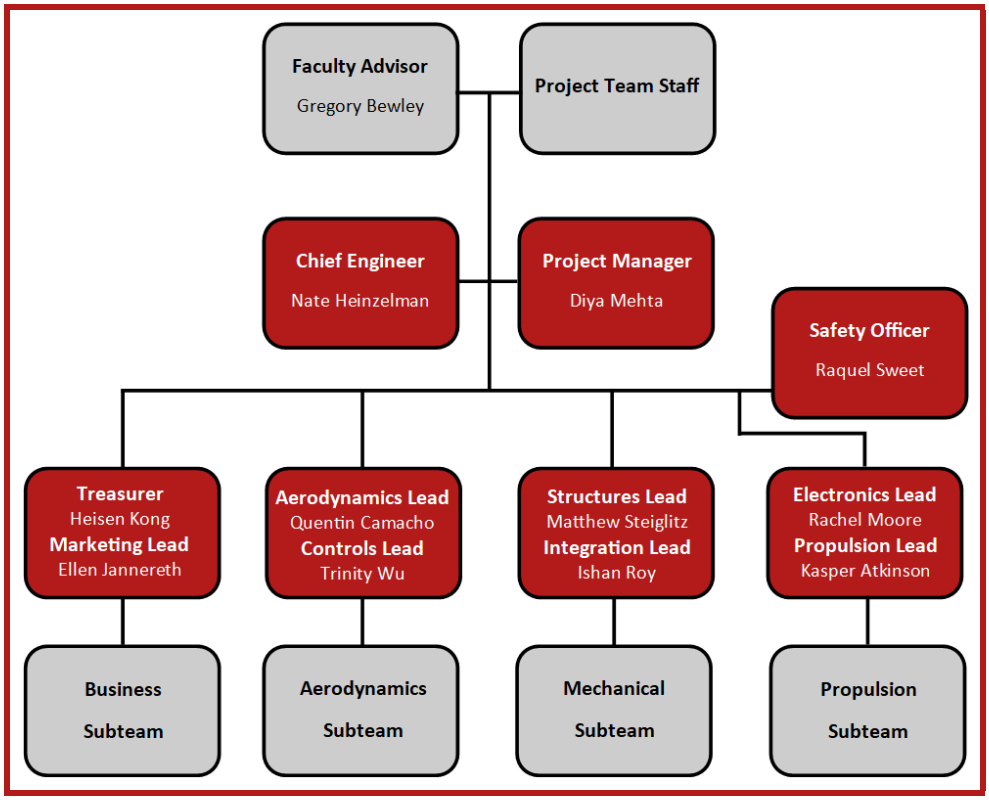

Figure 2.1.1: Team organization chart

2.2 Timeline and Milestones

A schedule of team operations was developed at the beginning of the academic year to guide the team through the competition timeline. To facilitate this, major projects and deadlines were put in the Gantt Chart in **Figure 2.2.1**. As the project progressed, alterations were made to the schedule, which are shown as the actual timing in the chart.

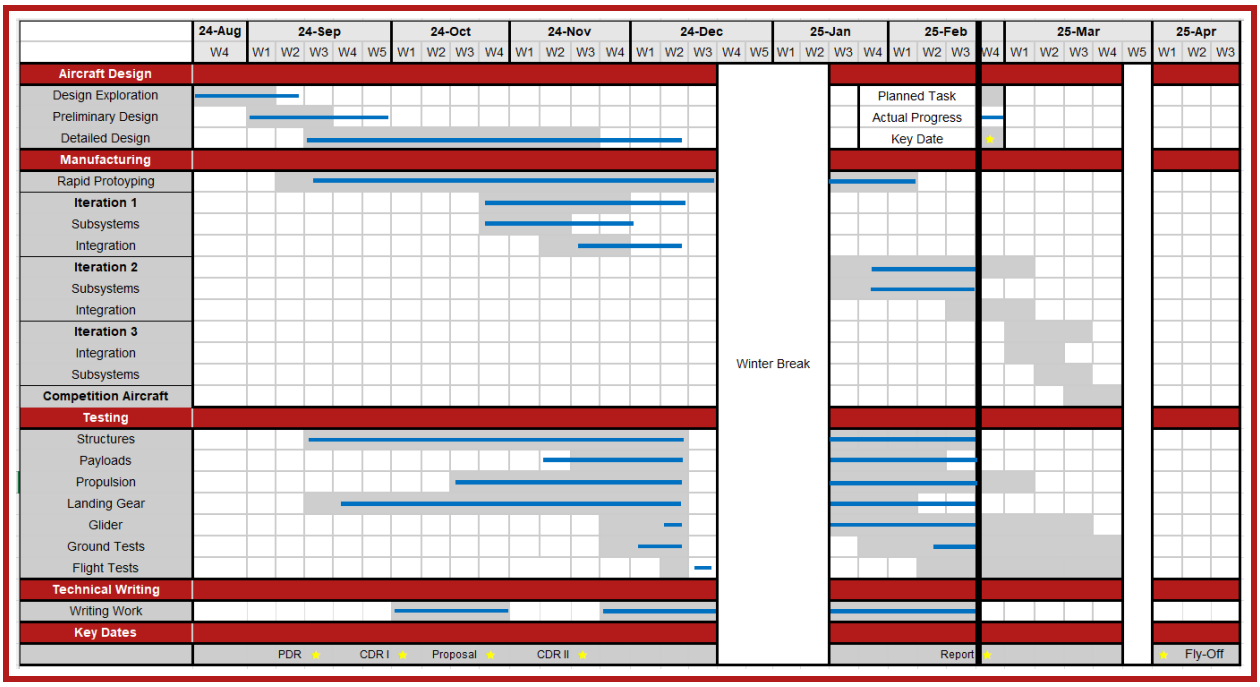

Figure 2.2.1: Gantt chart of scheduled and actual development

3 Conceptual Design Approach

3.1 Mission and Design Requirements

3.1.1 Problem Statement

The theme of the 2024-2025 AIAA DBF competition is experimental supersonic aircraft testing. As such, the competition aircraft Yeägerflug is designed conceptually as a bomber that can be converted to a supersonic testbed. The aircraft will undertake three flight missions, including demonstrations of Yeägerflug's airworthiness (M1), its payload carrying capacity (M2), and its capability as an experimental aircraft testbed (M3). M3 also demonstrates the performance of the X-1 test vehicle during the autonomous flight phase. The ground mission (GM) will demonstrate the ease with which Yeägerflug can be transformed from a bomber to an experimental aircraft testbed. The team's objective is to design and manufacture Yeägerflug to achieve the maximum combined score across all missions.

3.1.2 General Requirements

Each flight mission begins in the staging box after which the ground crew is given five minutes to put the aircraft in the correct configuration for the mission. The three flight missions will have the aircraft follow the flight path shown

in **Figure 3.1.1**. In the allotted five-minute window, the aircraft must complete either three laps or as many laps as possible, depending on the mission. The time will begin once the throttle is advanced for the first take-off attempt. To successfully gain points for the mission, the aircraft must complete a landing after the end of the given time.

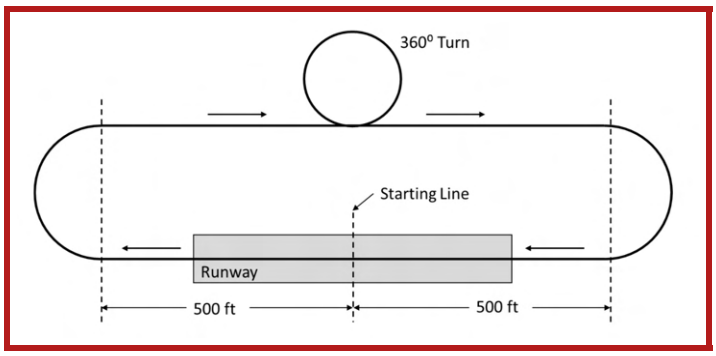

Figure 3.1.1: Flight pattern for all missions [1]

The total team score is a function of the design report score, proposal score, and total mission score. The function is given in **Equation 1**.

$$Total\ Score = (0.15 \times Proposal\ Score + 0.85 \times Design\ Report\ Score) \times (M1 + M2 + M3 + GM) + P \quad (1)$$

3.1.3 Mission Specific Requirements

Mission 1: Delivery Flight The first mission is a delivery flight in which the aircraft flies without the payload. The mission objective is to complete three laps within five minutes. The time begins when the throttle is first advanced and is completed when the aircraft passes over the finish line. Mission 1 is scored on completion according to **Equation 2** below.

$$M_1 = \begin{cases} 1 & \text{Successful mission} \\ 0 & \text{Unsuccessful mission} \end{cases} \quad (2)$$

Mission 2: Captive Carry Flight The second mission is a demonstration of the capacity of the aircraft to carry the payload. Both fuel tanks, which are loaded, and the X-1 test vehicle are attached to the aircraft. The objective of this mission is to fly three laps while maximizing load and minimizing flight time. The scoring is given by **Equation 3**, where $\text{Max}_{\text{fuel weight/time}}$ is the maximum ratio of payload weight to flight time for any team.

$$M_2 = 1 + \left[\frac{\text{N}_{\text{fuel weight / time}}}{\text{Max}_{\text{fuel weight / time}}}\right] \quad (3)$$

Mission 3: Launch Flight The third mission is a demonstration of the X-1 test vehicle. The aircraft carries the fuel tanks and the test vehicle, launching the test vehicle mid-flight. The objective for this mission is to maximize the number of laps flown within five minutes as well as for the test vehicle to land in a designated target area, as shown in **Figure 3.1.2**. This mission is scored according to **Equation 4**, which includes bonus points for an accurate landing of

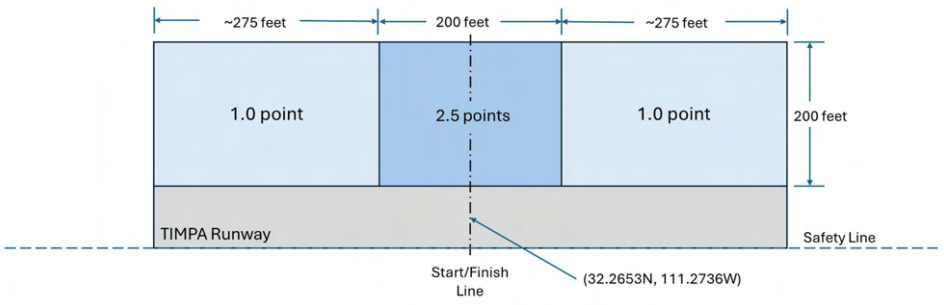

Figure 3.1.2: Bonus point landing zones for M3

the test vehicle, where Max $\left(\#\text{ laps flown} + \frac{\text{bonus box score}}{\text{X-1 test vehicle weight}}\right)$ is the maximum laps and bonus points that any team achieves.

$$M_3 = 2 + \left[\frac{\text{N}_{\#\text{ laps flown}+\frac{\text{bonus box score}}{\text{X-1 test vehicle weight}}}}{\text{Max}_{\#\text{ laps flown}+\frac{\text{bonus box score}}{\text{X-1 test vehicle weight}}}}\right] \tag{4}$$

Ground Mission: X-1 Flight Test Program Demonstration The purpose of the ground mission is to demonstrate the efficiency with which Yeägerflug can be converted from a bomber into a test aircraft. This includes the installation of all payloads and a ground test launch of the test vehicle. The aircraft enters the staging box with all payloads removed, and the installation of every component is timed. The objective for this mission is to minimize the assembly time, which is scored according to **Equation 5**, where $Min_{missiontime}$ is the lowest mission time score of all teams.

$$GM = \left[\frac{\text{Min}_{\text{Mission Time}}}{\text{N}_{\text{Mission Time}}}\right] \tag{5}$$

3.1.4 Mission Requirements Decomposition

This section outlines the requirements and constraints for the four missions of the 2025 Design Build Fly Competition. These design requirements form the basis of the aircraft design space and inform all major design decisions. They include external requirements as stipulated in the rules [1] as well as internal ones derived from those rules. The mission requirements have been deconstructed and translated into a set of system requirements that each subsystem must meet. A comprehensive breakdown of the requirements the aircraft must achieve is contained in **Table 3.1.1**.

Req	#	Requirement Description
SIZE	1	The airplane's wingspan cannot exceed five feet.
SYS	1	No component shall be released from the aircraft during flight, except the X-1 test vehicle in M3.
	2	The aircraft shall complete a minimum of three laps within five minutes.
	3	The aircraft shall be prepared for flight within five minutes. .
	4	Aircraft must start in the staging box with the propulsion battery pack(s) removed.
	5	Aircraft must land successfully for a score to be counted.
AERO	1	The aircraft must generate sufficient lift for all flight missions.
	2	The control surfaces shall resist flutter while providing sufficient deflection to maintain aerodynamic control.
	3	The aircraft must not be in a rotary wing or lighter-than-air configuration.
	4	The aircraft must be laterally and longitudinally stable in flight.
MECH	1	There will be at most one internal fuel tank. All external fuel tanks must be the same.
	2	All external fuel tanks must be attached to the airplane securely using pylons.
	3	Pylons must be removable and not a permanent feature of the aircraft.
	4	The airframe must be able to support all mounted payloads, motors, and aerodynamic structures.
	5	The landing gear must support the expected stress of landing and the resting weight of the aircraft.
PROP	1	Brushed or brushless electric motors shall sustain flight for at least five minutes.
	2	The airplane shall use NiCad/NiMH or Lithium battery(ies).
	3	The aircraft shall have one or more motors and/or propellers.
	4	The propeller can be changed for each flight attempt.
	5	Energy for take-off shall come from the on-board propulsion battery pack(s).
	6	Each airplane will use a commercially produced propeller/blades.
	7	The airplane must have an externally accessible switch to turn on the radio control system. It cannot be internal or under a panel or hatch. An arming plug is not considered an acceptable switch. The radio control system switch must be separate from the propulsion system fuse & arming system.
	8	There can be a maximum of one battery pack connected to a propulsion system. A propulsion system consists of one battery, one externally accessible arming fuse, one or more electronic speed controllers (ESC), and one or more motors. If the ESC has a Battery Eliminator Circuit (BEC), it must be disabled.
	9	Propulsion power total stored energy cannot exceed 100 watt-hours.
	10	All battery packs must be unaltered and commercially procured as Commercial-Off-The-Shelf (COTS) battery packs. Custom battery packs will not be allowed.
	11	The maximum current rating for the Arming Fuse is 100 amps.
	12	Batteries may not be changed or charged during any mission attempt.
M2	1	There must be at least two externally mounted fuel tanks carried by the aircraft.
	2	Fuel tank must be an unmodified beverage bottle with screw cap with a minimum capacity of 16 oz.
M3	1	Aircraft must fly at least one lap in five minutes, then land.
	2	The X-1 vehicle must fly autonomously and land in the landing zone with lights on.
	3	The X-1 vehicle must be mounted below the fuselage between the left and right external fuel tanks with a minimum 0.25" clearance between the top of the test vehicle wings and bottom of the aircraft fuselage, wings, and outer surface.
	4	The X-1 vehicle must be securely attached during the entire flight, apart from launch.
GM	1	The pylons and fuel tanks must be installed without lifting the aircraft.
	2	The X-1 test vehicle must be installed and released.
	3	The X-1 test vehicle's lights must activate upon release.

Table 3.1.1: Aircraft requirements decomposition matrix

3.2 Scoring Sensitivity Analysis

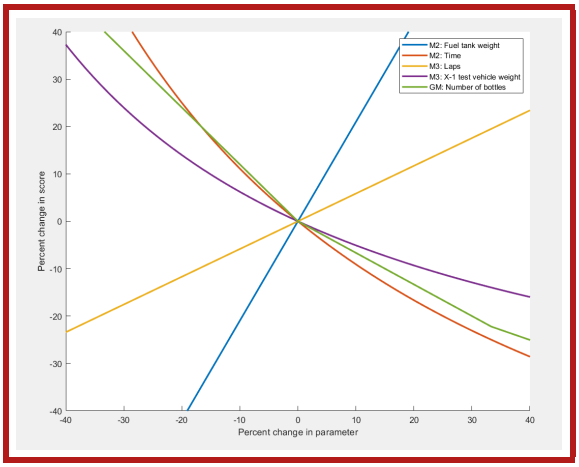

Figure 3.2.1: Sensitivity study results

In order to determine which of the mission parameters have the greatest impact on the overall competition score, a scoring sensitivity analysis was conducted in MATLAB [4] . Estimates for the average value of each mission factor were produced from a study of previous DBF competitions; these approximations were then used to calculate a baseline score. Additionally, the scoring system is heavily dependent on the highest score achieved by any team in each particular mission. It was assumed that at least one team will optimize for each mission, so the normalizations are based on the respective theoretical maximum scores within the design spaces. After the baselines were determined, each parameter was varied to investigate its sensitivity.

The results of this study are shown in **Figure 3.2.1**. The mass of the fuel tanks contributes most to the score, followed closely by the time of completion for M2, the number of fuel tanks, and finally, the mass of the X-1 test vehicle. The opposing impacts of the fuel tank weight and the number of fuel tanks carried indicate that the weight of each individual tank should be maximized.

Furthermore, minimizing the weight of the X-1 test vehicle is critical for maximizing the score. Finally, the number of laps completed in M3 is directly proportional to the score; this indicates that flying as quickly as possible without dropping below a five minute flight time is desirable. These results were used to guide the design process.

The scoring functions used in this sensitivity study were used to identify the optimal fuel tank mass, glider mass, and mission cruise velocities to maximize the competition score. Each parameter was given a range of possible values, and the projected score for every combination was calculated. Simultaneously, the script sized aircraft for these parameters. Many of these scoring parameter combinations were not physically realizable aircraft, and were thus discounted. Of the remaining contenders, the highest scoring had a fuel tank mass of 4.19 lb, divided across two tanks, an M2 time of 1.16 minutes, 7 M3 laps, and an X-1 test vehicle mass of 0.49 lb. A further description of the simultaneous sizing process that yielded these results is contained in **Section 4.2**.

3.3 Configuration Selection and Trade Studies

The aircraft shape was initially developed by considering a range of designs that meet the requirements given in **Table 3.1.1**. Trade matrices were created by assigning numeric values to the design parameters of individual aircraft elements, with possible configurations assigned a score from one (worst) to five (best) based on a weighted average. Weights were assigned by the team based on the relative importance of each design parameter to the subsystem in question. More important factors were given higher weights to ensure that they impacted the overall score more significantly than less important design considerations. Following this, the preliminary design process utilized trades decisions to design subsystems before completing the final design.

The following trade studies will be conducted by first considering relevant design requirements, then discussing potential implementations within the Yeägerflug and X-1 test vehicle. Out of those possibilities, the highest ranking configurations were chosen. Abbreviations used: Efficiency (Eff) and Configuration (Config).

3.3.1 Mechanical Structures Trades

Aircraft Structure The overall strength, size, and weight of the aircraft is affected by its structural configuration and airframe design. For M2 and M3, the aircraft structure must be able to support loading due to payloads mounted at various positions along the overall airframe. These payloads could be mounted away from the aircraft's centerline, inducing a large moment on the aircraft wings and body and necessitating a strong airframe. Additionally, the structural layout must be aerodynamic to ensure adequate airspeed and flight performance. As with any major system, manufacturability must also be factored into the design considerations of the airframe.

A single boom design consists of a single tail spar running along the longitudinal length of the aircraft. While this design is lightweight and streamlined, it lacks support along the lateral axis and hands off a significant portion of the structural loading due to payloads to the wings. Conversely, a twin-boom design consists of two tail spars running the length of the longitudinal axis of the aircraft separated by some distance. This design necessitates a wider aircraft with a less streamlined shape, but adds support in the lateral direction, away from the centerline of the aircraft. This characteristic benefits designs that require heavy payloads mounted far from the aircraft's centerline and was chosen for this reason.

Config (*Multiplier*)	Strength (*0.3*)	Weight (*0.25*)	Aerodynamics (*0.25*)	Manufacturability (*0.2*)	Total
Single-Boom	3	5	5	5	4.4
Twin-Boom	5	4.5	4.5	5	4.75

Table 3.3.1: Comparison of single-boom and twin-boom configurations

Fuselage Configuration The design of the fuselage significantly affects the cost, strength, and weight of the aircraft. The fuselage must balance strength to support structural and aerodynamic loads, weight and shape to improve flight performance, and overall size to ensure adequate space for electrical components and the launch system for the X-1 test vehicle. Manufacturability and cost must also be considered in order to produce a practical design due to the difficulty of working with some of the possible materials and their relatively high cost compared to the costs of other subsystems on the aircraft.

A rigid frame fuselage features a sturdy internal truss structure that bears all airframe loads, with the outer covering providing no significant structural support. While it is strong and easy to manufacture, the design is also heavy and provides less internal space than other options.

Semi-monocoque and monocoque fuselages are both stressed-skin designs. A semi-monocoque fuselage is easier to manufacture and is stronger than a monocoque but has significantly reduced internal space. While the monocoque fuselage is the weakest and hardest to manufacture, it was ultimately selected in order to minimize weight and maximize internal space. Additionally, the use of high strength materials can remedy this design's shortcomings in that area.

Material Selection for a Monocoque Fuselage An identical monocoque fuselage geometry will perform differently depending on the material used in its construction. Per aircraft mission requirements, high strength and low weight are preferred along with ensuring relative ease of manufacturability.

Wood is inexpensive and easy to work with, but its strength-to-weight ratio is far below that of composite materials. When comparing composites, fiberglass (GFRP) is the least expensive and easiest to work with but has a low strength to weight ratio. Therefore, despite being relatively expensive and difficult to work with, carbon fiber reinforced

Config (*Multiplier*)	Strength (*0.25*)	Weight (*0.3*)	Volume (*0.25*)	Manufacturability (*0.2*)	Total
Rigid Frame	5	2	3	5	3.6
Semi-monocoque	4	3	4	5	3.9
Monocoque	3.5	5	5	4	4.4

Table 3.3.2: Fuselage configuration trade matrix

polymer (CFRP) was ultimately selected due to its high strength-to-weight ratio. The team also investigated CFRP manufacturing techniques and determined it was feasible to use this material on the aircraft.

Material (*Multiplier*)	Strength/Weight Ratio (*0.5*)	Manufacturability (*0.25*)	Cost (*0.25*)	Total
Basswood	1	4	5	2.8
CFRP	5	3.5	3	4.1
GFRP	3	4	4	3.5

Table 3.3.3: Fuselage material trade matrix

Landing Gear Configuration Two landing gear configurations were compared: a four-wheel taildragger and a tricycle design. Stronger gear can support heavier loads, leading to increased mission scores. Ground clearance is required for the test vehicle to be mounted below the fuselage. Ground stability and reliable performance are essential for a successful takeoff and landing, as failure in either results in no mission score. Manufacturability must also be accounted for in order to produce a practical design.

The taildragger configuration has two large front wheels and two small rear wheels (one at the rear of each boom) supporting the load, while the tricycle configuration has one small front wheel and two large rear wheels. While tricycle is typically more stable than taildragger, the unique four-wheel taildragger design provides four points of contact with the ground and a large lateral distance between each wheel, making the aircraft more stable even under high loads. Tricycle gear allows for better ground clearance, but the taildragger's clearance was more than sufficient for the X-1 test vehicle and payloads. Finally, while the tricycle's powered nosewheel steering can more effectively steer the aircraft on the ground, the aircraft only needs to take off and land rather than taxi. The P-factor is negated by counter-rotating propellers, enabling the rudders to have enough control authority to steer the aircraft during takeoff and landing. Complicated nosewheel steering is also harder to manufacture and more likely to fail than a purely mechanical taildragger configuration. The taildragger configuration was ultimately selected due to its superior strength, stability, and reliability.

Config (*Multiplier*)	Clearance (*0.2*)	Steering (*0.1*)	Stability (*0.5*)	Reliability (*0.2*)	Total
Taildragger	4	3	5	5	4.6
Tricycle	5	5	4	3	4.1

Table 3.3.4: Landing gear configuration trade matrix

Fuel Tank Configuration According to the sensitivity analysis, increasing the weight had a more positive impact on the score than the decrease in velocity up to a certain point. It was found that four external tanks, though maximizing fuel weight, would reduce velocity enough to decrease the M2 score. Additionally, mounting the fuel tanks further outboard would decrease roll stability and increase loading on the wing, resulting in inferior handling characteristics and necessitating a heavy and bulky wing design. Ultimately, it was decided that two external tanks were the best choice to optimize the tradeoff in weight and speed, maximizing the M2 score. This design, combined with thoughtful fuel material selection, was ultimately chosen in order to maximize the M2 score. Additionally, minimizing the number of external fuel tanks and forgoing an internal one increases GM score by reducing the assembly time.

The addition of an internal tank would require a larger and heavier fuselage in addition to adding more weight to the overall aircraft. This configuration increases payload weight but at the cost of a large speed reduction, leading to an overall decrease of the M2 score. As such, it was determined that an internal fuel tank was not beneficial.

Config (*Multiplier*)	Fuel Weight (*0.4*)	Aircraft Speed (*0.4*)	Aircraft Handling (*0.2*)	Total
Two external tanks	4	5	5	4.6
Four external tanks	5	3.5	3	4.0
Internal tank	4.5	3.5	5	4.2

Table 3.3.5: Payload configuration trade matrix

X-1 Test Vehicle Flight To control the X-1 test vehicle, a GPS and autopilot system emerged as the best choice. Controlling a set of elevons, this configuration offers maximum reliability. An alternative considered was purely mechanical, where the test vehicle's wings are fixed at a spiral-inducing angle. However, this approach offered too much uncertainty, as wind speeds and direction would greatly affect its trajectory. A designated autopilot could be set to glide to the runway coordinates, adjusting flight trajectory as necessary.

Config (*Multiplier*)	Accuracy (*0.6*)	Complexity (*0.1*)	Weight (*0.3*)	Total
Autopilot	5	2	1	3.5
Fixed Deflection	1	4	5	2.5

Table 3.3.6: X-1 test vehicle flight control trade matrix

X-1 Test Vehicle Launch Mechanism The performance of the test vehicle's launch mechanism is crucial to the success of M2 and M3. The most important design considerations are reliability of operation, weight, and structural integrity. An optimal design will optimize strength for M2 and M3, reliability of operation for M3, and will be low in weight to improve aircraft speed and flight duration in all missions. The launch mechanism must be strong, simple, and lightweight.

In the initial design phase, a linear actuator-based design was considered in which the actuator would retract a pin from a tab in the test vehicle's fuselage, thereby releasing it. While this mechanism would be lightweight, the actuator's complexity and the gravity-based launch procedure would result in a less reliable design. Preliminary prototyping also showed that the actuator-based design was difficult to manufacture due to the intricate nature of the mechanisms needing to be 3D-printed.

With the lever-arm based design, the X-1 test vehicle slots into a launch arm attached to a servo motor that can be configured to a variable angle. The test vehicle can only move along the axis of the arm, leading to a more reliable launch.

Mechanism (*Multiplier*)	Reliability (*0.4*)	Weight (*0.3*)	Strength (*0.3*)	Total
Linear Actuator	2	5	2	2.9
Electromagnet Drop	2	4	4	3.2
Lever Arm	5	4	5	4.7

Table 3.3.7: X-1 test vehicle launch mechanism trade matrix

The use of a 3D-printed mechanical launch arm to attach the test vehicle also resulted in a stronger, cheaper, and more reliable mechanism while minimizing weight. Because of its optimal performance across all parameters, this design was ultimately selected for the test vehicle launch mechanism.

An electromagnet drop was also considered before Q&A 1 was released. However, this design was ruled out due to reliability concerns and the lack of a mechanical attachment to the X-1 test vehicle.

3.3.2 Aerodynamics Trade Studies

Wing Location Configuration The wing location of an aircraft has an effect on aircraft stability and aerodynamic performance. The missions set clearance requirements that are dependent on the wing height. Wing location also impacts fuselage capacity, however Yeägerflug is not required to carry large payloads so fuselage capacity was not considered for selecting a configuration.

The high-wing configuration has the wing mounted at the top of the fuselage providing a pendulum effect that stabilizes the roll of the aircraft. A low-wing configuration has the wings mounted at the bottom of the fuselage providing less stability but improving turn rate and improving takeoff/landing performance from larger ground effects. A mid-wing configuration provides a compromise between high-wing and low-wing performance characteristics while supporting a more robust integration with a small fuselage. Ultimately a mid-wing configuration was chosen because it provided favorable aerodynamic characteristics without requiring significant reinforcement to integrate into the fuselage.

Config (*Multiplier*)	Aerodynamics (*0.3*)	Integration (*0.4*)	Course (*0.1*)	Manufacturing (*0.2*)	Total
High-Wing	3	2	4	3	2.7
Mid-Wing	4	4	3	3	3.7
Low-Wing	3	2	2	3	2.5

Table 3.3.8: Wing location configuration trade matrix

Wing Taper Integration is deemed to be a very important aspect of design throughout the requirements as for all missions the plane needs to be prepared for flight within 5 minutes. The two choices considered were to have a taper or no taper on the wing.

An untapered wing would have less aerodynamic efficiency compared to a tapered wing. Though, the manufacturability and integration of the entire aircraft was found to be much more difficult with a taper. Ultimately, the

untapered wing was chosen due to manufacturing and integration simplicity outweighing the slight increase in efficiency. It was also found that the excessive chord at the tip of the untapered wing would have caused the wing to generate more lift toward the top than is ideal [7].

Config (*Multiplier*)	Aerodynamics (*0.35*)	Missions (*0.15*)	Manufacturing (*0.5*)	Total
Taper	4	3	3	3.4
No Taper	3	4	4	3.7

Table 3.3.9: Wing taper configuration trade matrix

Flap Configuration The configuration of the flaps on the aircraft has effects on aerodynamic control, pilot control, and manufacturability. Due to the unlimited takeoff distance the aircrafts ability to takeoff in a short distance was not an emphasized parameter, instead manufacturability was prioritized. The three configurations under consideration were ailerons and flaps, flaperons, and ailerons only.

Separate ailerons and flaps were determined to be the most advantageous aerodynamically, as the wing camber would not limit the ailerons' available deflection. Flaperons balanced all three parameters as they maintained the advantages of simpler manufacturability while increasing aerodynamic control at lower airspeeds. However, no flaps were determined to be the best configuration as they excelled in manufacturability and programmability, with the lower aerodynamic control at lower airspeeds not having any effect on mission scores.

Config (*Multiplier*)	Aerodynamics (*0.2*)	Programmability (*0.3*)	Manufacturing (*0.5*)	Total
Ailerons and Flaps	5	4	2	3.2
Flaperons	4	3	5	4.2
Ailerons with No Flaps	3	5	5	4.6

Table 3.3.10: Flap configuration trade matrix

Wing Leading Edge Configuration The design of the aircraft required sufficient lift for all mission configurations and should be as efficient as possible to lower mission, in turn increasing mission scores. The wing's leading edge has a large effect on both of these factors, and therefore needed to be configured in a way that would best preserve the shape of the chosen airfoil.

Various wing leading edge configurations were assessed for the aircraft: stringers, balsa sheet, and foam. Stringers had the highest manufacturing score due to having the simplest implementation procedure. However, the stringers led to an inconsistent surface at the leading edge and necessitated a hardwood comb, resulting in a lower aerodynamics score. The balsa sheet provided a smooth and continuous leading edge, which improved aerodynamic performance by decreasing flow separation. The low-complexity of the balsa sheet's manufacturing procedure involved shaping the sheets after exposure to hot water. The foam leading edge held the shape of the airfoil but at a higher weight than the balsa method. Also the foam leading edge deformed slightly when heated during the MonoKote application process.Due to its relative simplicity and excellent aerodynamic performance, a curved balsa sheet leading edge was identified as the best option.

Config (*Multiplier*)	Aerodynamics (*0.6*)	Manufacturing (*0.4*)	Total
Stringers	3	5	3.8
Balsa Sheet	5	4	4.6
Foam	4	2	3.2

Table 3.3.11: Wing leading edge trade matrix

Control Surface Actuation Configuration The control surface actuation has effects on the control characteristics of the control surfaces of the aircraft. The actuation has to be able to reliably achieve accurate and repeatable deflection in accordance with the pilot's control inputs while minimizing manufacturing complexity. The three configurations considered for the aircraft's control surfaces were internal, hybrid, and external. The internal configuration had the best aerodynamic characteristics due to its fully enclosed design which minimized drag. The external configuration maximized control surface deflection due to the absence of structural constraints like the rear comb, providing superior maneuverability during flight missions. The hybrid configuration emerged as the favored choice, combining the average aerodynamic performance with maximum deflection capability and acceptable manufacturing requirements. It scored equally as well as the external configurations for its manufacturing score, as the hybrid configuration required careful alignment of both internal and external components. An example of the hybrid configuration is shown in Figure **Figure 3.3.1**.

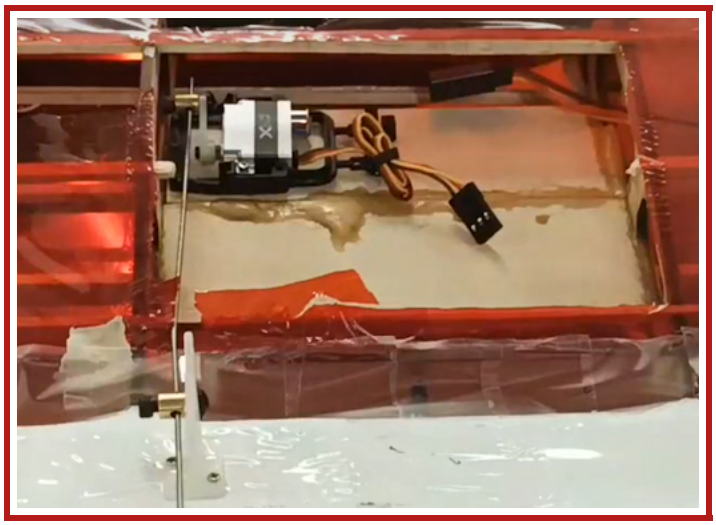

Figure 3.3.1: Hybrid control surface configuration

Config (*Multiplier*)	Aerodynamics (*0.2*)	Degrees of Deflection (*0.4*)	Manufacturing (*0.4*)	Total
Internal	5	3	1	2.6
Hybrid	4	5	3	4.0
External	3	5	3	3.8

Table 3.3.12: Control surface actuation configuration matrix

Tail Configuration The tail configuration has significant effects on the control, stability, and structural integrity characteristics of the aircraft. The tail has to be able to integrate with the twin-boom aircraft structure without diminishing any of the aforementioned characteristics. The four configurations considered for the tail were the conventional tail, T-tail, twin-boom tail, and boom-mounted inverted V-tail. The stability and control characteristics of each configuration were factored into the aerodynamic score, with all but the boom-mounted inverted V-tail performing equally as well. The conventional and T-tail suffered in integration as they are conventionally more suited to use on single-boom aircraft. The conventional and twin-boom tail scored best in manufacturability as their vertical and horizontal stabilizers have the highest structural stability, rigidity, and ease of integration with each other. The twin-boom tail emerged as the favored configuration, with the primary advantage being that it would seamlessly integrate with the twin-boom aircraft structure. Notably for the boom-mounted tail, the vertical tail end-plate effect improves the aerodynamic performance of the horizontal tail [6].

Config (*Multiplier*)	Aerodynamics (*0.3*)	Integration (*0.3*)	Manufacturing (*0.4*)	Total
Conventional Tail	4	2	4	3.4
T-Tail	4	2	3	3.0
Twin-Boom Tail	4	4	4	4.0
Boom-Mounted Inverted V-Tail	3	4	2	2.9

Table 3.3.13: Tail configuration trade matrix

3.3.3 Propulsion Trade Studies

Motor For the motor arrangement, a primary driver was the scoring in **Section 3.2**. With mission completion time as an important factor in score maximization, cruise efficiency and velocity emerged as priorities. Wing-mounted motors had the benefit of directing air over the wings, increasing flight efficiency [14]. This configuration also provided more thrust, resulting in a greater mission cruise velocity. While a single motor would weigh less, this trait was not as pertinent to mission score.

A secondary factor was the previously decided twin-boom configuration. Best suited to this preliminary aircraft design were twin-tractor motors. Two motors could better utilize the structural support provided by the tail spars of the twin-boom configuration. Consequently, a twin tractor motor configuration was decided upon.

Config (*Multiplier*)	Eff. (*0.3*)	Weight (*0.1*)	Velocity (*0.3*)	Stability (*0.2*)	Integration (*0.1*)	Total
Single Tractor	2	5	4	3	3	3.2
Twin Tractors	3	3	5	5	5	4.2
Twin Pushers	4	2	3	4	2	3.3

Table 3.3.14: Propulsion configuration trade matrix

4 Preliminary Design

4.1 Design and Analysis Methodology

The team utilizes an iterative design and analysis approach modeled on the systems engineering approach used by the aerospace industry. The development process, including all aspects of the design, build, and flight phases, is depicted in **Figure 4.1.1**. A thorough and detailed reading of the competition rules sent out in August allowed all team members to understand the mission requirements, leading to the development of sub-system requirements as shown in **Section 3.1.4**. These requirements provided a list of quantitative and qualitative items that needed to be fulfilled either through design or through ground or flight testing. The subsystem requirements are further distilled in a set of trade studies that analyze the viability of different aircraft configurations. The main objective of these trade studies was to define the overall aircraft geometry and what the aircraft should generally look like before going into further detail about exact dimensions. Additionally, the team developed a MATLAB scoring sensitivity script to gain a better perspective of the different objectives and what should be optimized for this year's aircraft. A preliminary design review concluded the conceptual design phase.

The sub-system requirements and results of the scoring sensitivity script allowed the team to progress to the preliminary design phase. Notably, a separate MATLAB sizing script, aerodynamic analysis utilizing XFLR5 [13], and propulsion simulations using eCalc [5], were generated to determine quantitative benchmarks and design dimensions the aircraft needed to meet. Additionally, a constraint analysis and drag predictions were used to determine our design space. These results helped refine the designs proposed in the conceptual design phase and develop subsystem and system computer-aided design (CAD) models in SOLIDWORKS [10]. Subsystem and system critical design reviews allowed for team members and alumni to provide input and feedback before concluding the preliminary design phase and transitioning to fabrication and manufacturing. Feedback from subsystem and flight tests allows the team to identify critical areas of improvement and propose solutions for future iterations. This allows an iterative design and analysis process where future iterations and prototypes improve on prior designs and lead to increased efficiency and higher flight scores.

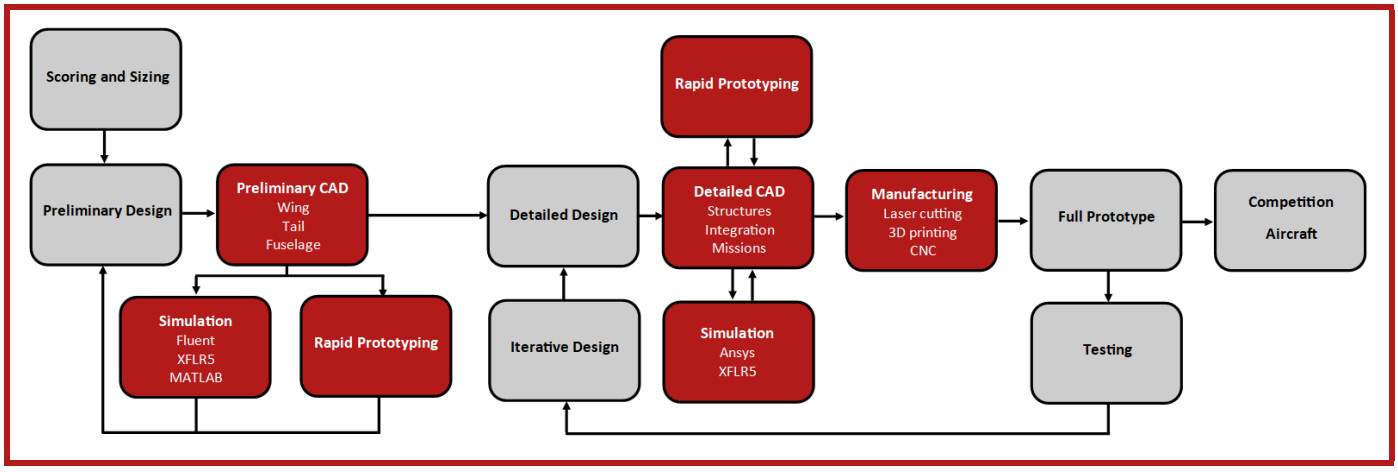

Figure 4.1.1: Design process and procedures

4.2 Aircraft Sizing Procedure

In order to determine the optimal design based on the competition rules, the team took a multidisciplinary design optimization approach. This project involved creating a sizing script in MATLAB, with mathematical models describing the behavior of the aircraft subsystems. Some specific examples of modeled interactions include the number of external fuel tanks impacting the coefficient of parasitic drag and the area of the wing impacting the structural mass of the aircraft.

For the optimization, two major design variables were identified: the aspect ratio of the wing and the power of the propulsion system. Both of these are directly controlled and fundamentally change the performance of the aircraft. For every combination of these two variables, the performance of the aircraft was calculated, including the projected score on each mission. These scores are shown in the contour plot in **Figure 4.2.1**. Additionally, the contours of the projected M3 cruise velocity are overlaid. The best performing combination is marked with a yellow star.

Several equations were used in the sizing script. The main aerodynamic equation, **Equation 6**, links the aspect ratio of the wing to the coefficient of drag. This equation additionally connects to the power required by describing the drag that the thrust must overcome. As such, it serves as the basis of the optimization script.

$$C_d = C_{d0} + \frac{C_l^2}{\epsilon AR} \tag{6}$$

Additionally, the power was incorporated into the flight model by **Equation 7**. In this model, it is assumed that the electric power is converted into the mechanical power needed to overcome drag, with some efficiency factor epsilon.

$$\epsilon P = TV \tag{7}$$

These equations were used to solve for the performance of all potential aspect ratio and power combinations. Using the assumption of steady flight, where thrust balances drag and lift balances weight, the equations were solved iteratively for the cruise velocity until these conditions were satisfied. The cruise velocity, as well as the mass of the design combination, was plugged into the scoring functions used in the sensitivity analysis above to generate the predicted competition performances across the design space.

A major goal of this study was to determine what design philosophy would be the most successful in this year's competition. The results show that there are two peaks in score, corresponding to a fast, light aircraft optimized for M3 and a slow, heavy aircraft optimized for M2. To minimize the complexity of the design, and to take advantage of the slightly higher predicted score, the team opted to pursue an aircraft in line with the first design philosophy. This led to an aspect ratio of 6.48. The results show that increasing the propulsive power of the aircraft benefits the projected score in all cases. As such, the team opted to use the largest power system allowed within the constraints laid out in the rules

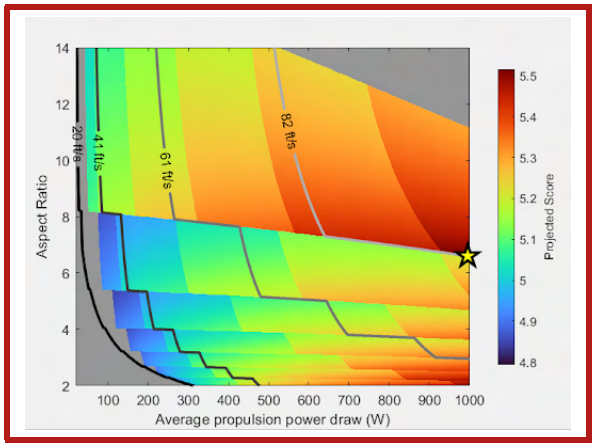

Figure 4.2.1: Projected score contour plot as a function of aspect ratio and power draw

4.2.1 Wing Sizing

One of the design constraints imposed by this year's rules was a maximum wingspan of 6.00 ft, (SIZE 1 in **Table 3.1.1**). With the aspect ratio determined by the process described in the previous section, the wingspan was the remaining parameter to change the wing area. By maximizing the wing area, the aircraft can carry a heavier load, improving the M2 performance. As such, the wingspan was set at 69.00 in. This was three inches less than the imposed constraint, which provided a margin of error against failing to satisfy the requirement. Combined with the aspect ratio of 6.48, this yielded a wing chord length of 10.65 in. Additionally, to maximize the wing surface area, a taper ratio of 1 was used. Although a stronger taper can improve efficiency, the inclusion of the wingtip devices made a taper redundant.

Parameter	Value
Wing area	5.06 ft^2
Wingspan	69.00 in
Chord length	10.65 in
Aspect ratio	6.48
Taper ratio	1.00

Table 4.2.1: Aircraft wing dimensions

With these parameters, the area of the wing was 5.06 ft^2 . In its different configurations, the mass of the aircraft ranges from 7.45 lb to 12.35 lb. This equated to a wing loading of between 23.56 oz/ft^2 and 39.05 oz/ft^2. With the design focus on cruise, this range indicated a fast and light aircraft, validating the analysis conducted in the previous section. This configuration gives the aircraft a maximum takeoff weight of 12.35 lb. The empty aircraft is estimated at 7.45 lb, giving.

4.2.2 Empennage Sizing

The empennage provides static and dynamic stability as well as giving control to the pilot to pitch and yaw. The tail was sized using volume coefficients as described by Raymer [7]. Approximating the aircraft as a general aviation twin-engine aircraft, gives horizontal and vertical volume coefficients of 0.80 and 0.07 respectively, and provides a starting point of the empennage sizing process.

$$V_H = \frac{S_H l_H}{S_w \bar{c_w}} \tag{8}$$

$$V_V = \frac{S_V l_V}{S_w b_w} \tag{9}$$

A major parameter of the empennage is the distance between the empennage and the wing. To maintain static stability and to provide space for the test vehicle, the tail arm is set to 27.56 in. Through iterative simulation, this was identified as the tail arm that provides an optimal static margin. Using the volume coefficients, this tail lever arm sets the required surface areas of the horizontal and vertical stabilizers. The area of the vertical stabilizer is evenly divided across the two components of the H-tail. Additionally, the aspect ratios for the two stabilizers are set to 2.91 and 1.50, respectively. These aspect ratios are within the estimates of aircraft flying similarly sized payloads from previous years' competitions. A taper was implemented for the vertical stabilizers to improve aerodynamic efficiency and to reduce empennage mass. This was not included on the horizontal stabilizer to ensure stable integration with the tail booms. Both stabilizers utilize a symmetrical NACA 0012 airfoil, allowing for equal control in both directions. Empennage control surfaces consist of an elevator on the horizontal stabilizer and rudders on the vertical stabilizers. Their chord lengths are set based on an analysis of similar aircraft from previous competitions. The elevator is 25% of the horizontal stabilizer chord and the rudders are 40% of the vertical stabilizer chord. **Table 4.2.2** summarizes the geometric parameters of the empennage.

Stabilizer	Horizontal Stabilizer	Vertical Stabilizers
Airfoil	NACA 0012	NACA 0012
Tail lever arm	27.56 in	38 in
Planform Area	246.08 in^2	64.71 in^2
Aspect Ratio	2.91	1.50
Taper Ratio	0	0.78
Span	27.56 in	9.84 in
Root Chord	9.47 in	7.72 in
Tip Chord	9.47 in	5.43 in

Table 4.2.2: Preliminary sizing of empennage design

4.2.3 Powerplant Sizing

The aircraft's propulsion system is relatively unconstrained by this year's competition rules. Iterative simulation was conducted with eCalc, coupled with market availability analysis, to determine the most effective and attainable configuration to achieve the team's goal of maximizing power draw for the three flight missions.

To size the propulsion system, eCalc's online calculator, propCalc, was used. This year, a Python program [11] was developed to iteratively evaluate numerous propulsive configurations. Accessing the propCalc page directly, the script uses user-inputted battery and motor parameters. The program then optimizes the propeller configuration for all viable setups. A CSV file is created with all possible configurations, including the expected static thrusts, current draws, and flight times of each. Following the use of eCalc, in-house testing allowed the team to reach a finalized decision.

The propulsion system must also be able to accommodate the projected flight times calculated in the scoring analysis. Most importantly, in order to maximize the number of laps that the aircraft can complete in M3, it must be able to fly for the entire allotted five minute flight window, while flying quickly. As such, the motors must be able to utilize all of the energy stored within the battery during this flight window. In M1 and M2, maximizing flight time is not a concern, so the motor must also be able to draw power from the battery more quickly, allowing higher speeds during these missions. These competing demands were analyzed with eCalc to determine the best propulsion system.

Battery Sizing Aircraft battery selection prioritized the propulsion system's thrust-to-weight ratio, flight time, and integration in order to maximize mission score. Comparing battery voltages, charge capacity, and C-ratings, one variable was changed while all others were held constant. These combinations were processed and ordered through the eCalc iterator program, facilitating comparison by extracting pertinent data.

Following the analysis, a single 6S1P lithium polymer (LiPo) battery was identified as the highest-performing category. While using two batteries simultaneously offers more thrust, a single battery provides a flight time appropriate for all missions while decreasing wiring complexity. With a 4500 mAh capacity, these batteries are 99.9 Wh, close to the 100 Wh competition-set maximum. Their comparison is further detailed in **Table 4.2.3**.

Type (*Multiplier*)	Thrust-weight (*0.3*)	Flight time (*0.3*)	Integration (*0.2*)	Attainability (*0.2*)	Total
8s 3300mAh	5	4	5	1	3.9
2x 8s 1600mAh	5	4	3	5	4.3
6s 4500mAh	4	5	5	5	4.7
2x 6s 2200mAh	4	3	4	5	3.9

Table 4.2.3: Battery configurations comparison

Motor and Propeller Sizing Analyzing the predicted five and three minute mission flight times, **Equation 10** quickly narrowed the scope of necessary motor powers. Five minute and three minute flight times require 2000 W and 1200 W, respectively. Dividing the power between two motors, a motor wattage between 600 W and 1000 W was found the most desirable. Due to the chosen single-battery two-motor configuration, a key constraint is also the 100 A maximum current draw established by the competition rules. Consequently, each motor can receive at most 50 A. A 6S1P Lipo battery can output 1000 W to each motor in this configuration, affirming the previous calculations.

$$\frac{\text{Energy Capacity (Wh)}}{\text{Flight Time (h)}} = \text{Power Draw (W)} \tag{10}$$

It was quickly determined that the combination of two low KV and large diameter motors best suit these requirements. Inputting these preferences into the eCalc iterator program, top configurations were consistent with the high-speed design philosophy established in **Section 3.2**. The highest-scoring motor was the Cobra CM-4515/18, with multiple potential propeller combinations. **Figure 4.2.2** displays expected static thrusts and flight times as functions of propeller diameters and pitch which met current pull constraints. With a 14 in x 10 in propeller, the motor can pull 1000 W. However, 12 in x 12 in, 13 in x 11 in, and 15 in x 8 in propellers were also procured for further testing. This testing is further detailed in **Section 7.1.2**.

Component	Selected Specifications
Battery	4500mAh 6S1P 20/30C LiPo Battery
Motors	Cobra CM-4515/18
ESC	60 Amp ESC
Propeller	14 in x 10 in Propeller
Fuse	100 Amp Blade Fuse

Table 4.2.4: Propulsion specifications

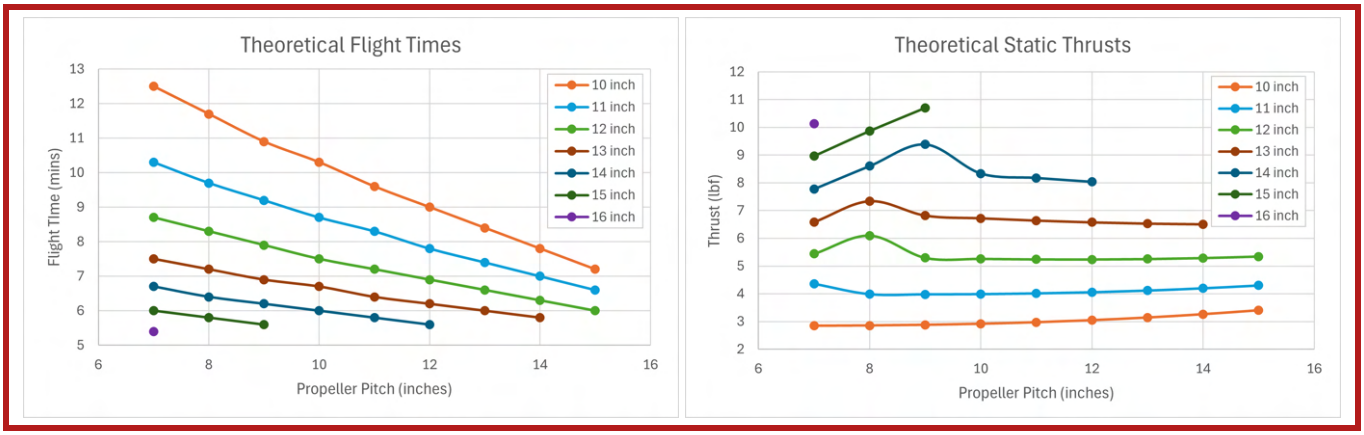

Figure 4.2.2: Theoretical flight times and static thrusts for given propeller pitches and diameters. Not all analyzed propellers were commercially available.

4.2.4 Test Vehicle Parameters

Wing Geometry Preliminary investigations into flight control systems for the X-1 test vehicle indicated that they would contribute a substantial amount of mass to the overall weight of the vehicle. As such, it was critical to size a test vehicle that could adequately support this mass. Gliders fly according to the relationship in **Equation 11**, where γ is the glide slope. To minimize this angle and prevent the X-1 test vehicle from descending too quickly, lift needs to be maximized.

$$\frac{D}{L} = tan(\gamma) \tag{11}$$

Increasing the surface area of the wing will increase the lift, so a driving goal of X-1 test vehicle sizing was maximizing the wing area. The wingspan is constrained by the other components on the wing of the main aircraft, so the test vehicle wingspan was set to 18.00 in, at the constrained limit. Decreasing the aspect ratio too much, while increasing surface area, will increase drag, so there is an optimal aspect ratio. The aspect ratio was set at 8.50 to minimize the glide ratio while maintaining the structural integrity of the test vehicle wing.

Empennage The key design consideration in the empennage of the X-1 test vehicle was simplicity. This led to a simple conventional tail design rather than a more complicated configuration. Additionally, the test vehicle is controlled with elevons rather than an elevator, so the empennage does not have any control surfaces. As such, the tail was designed to be blended into the fuselage, so it can be constructed as part of the same structure. The tail arm was set at 10.30 in so that the empennage is of the way of the release mechanisms, while not being overly long and increasing the mass of the vehicle. From this tail arm, the stabilizers were sized according to the volume coefficients process described in **Section 4.2.2** above. Following the simplicity principal, neither the vertical nor the horizontal stabilizer have airfoil profiles, instead they are rectangular for the ease of manufacturing.

Lights Strobe lights were promptly identified as favorable to continuous lights, to ensure visibility while in flight. LEDs were chosen for their energy efficiency and low weight. A battery pull-tab system, triggered by the test vehicle separation from the primary aircraft, was initially considered to activate the strobe lights. However, a magnetic-switch-controlled light system was recognized as the most dependable. Integrated into the dropping mechanism, the lights are activated and deactivated by the proximity of the magnetic switches, eliminating a mechanical movement that

could be compromised at drop speeds mid-flight.

Material Selection X-1 vehicle material selection prioritized minimizing weight due to the impact of the mass of the test vehicle on M2 and M3 scoring, and its impact on test vehicle controllability. Three preliminary design options were considered: a fully wooden build, a 3D-printed and wood hybrid, and a polystyrene foam design. While wooden and 3D-printed alternatives permit easier and more precise manufacturing, polystyrene foam weighs significantly less. After investigating foam manufacturing techniques through small-scale prototypes, the team found it was possible to manufacture an airframe for the test vehicle using foam and determined its lightweight properties made it the best choice.

4.3 Aircraft Analysis Procedure

4.3.1 Airfoil Selection

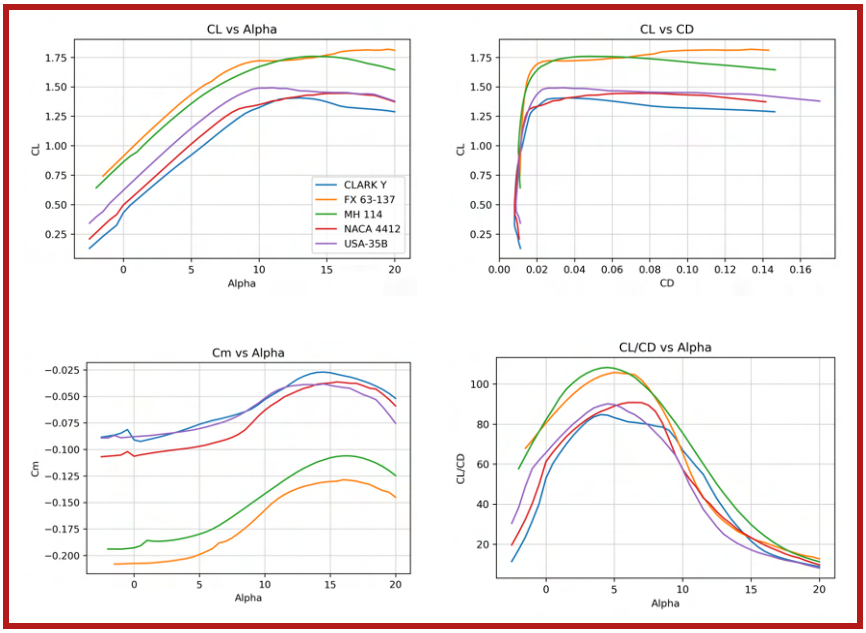

Figure 4.3.1: Clockwise from top left: Cl vs Alpha, Cd vs Alpha, Cm vs Alpha, Cl/Cd vs Alpha for various airfoils

Selecting an airfoil for the wing required the balancing of three important characteristics: lift performance, low drag, and ease of manufacturability. Based on these criteria, five airfoils were selected: CLARK Y, FX 63-137, MH 114, NACA 4412, and USA-35B. The performance curves of these airfoils analyzed in XFLR5 at a Reynold's number of 300,000 are shown in **Figure 4.3.1** below, and the key data for each airfoil is summarized in **Table 4.3.1** below. Both the FX 63-137 and the MH 114 stood out as strong candidates, performing consistently well in all aerodynamic metrics. However, the MH 114 has a relatively large camber which would be difficult to MonoKote. Thus after taking manufacturability into account, the FX 63-137 was the team's final decision, as its relatively large thickness provides sufficient space for internal components and structures while also facilitating manufacturing.

Airfoil	CL,max	CL,0	Stall angle (degrees)	CL/CD,max
CLARK Y	1.41	0.43	13.00	84.71
FX 63-137	1.72	0.91	10.00	105.78
MH 114	1.76	0.86	14.00	108.23
NACA 4412	1.31	0.50	8.80	90.74
USA-35B	1.49	0.62	10.50	90.13

Table 4.3.1: Airfoil data comparison

4.3.2 Static Stability and Flight Characteristics

In order to ensure that the aircraft is statically stable in flight, a static margin of -10% to -30% is desirable. This allows the aircraft to return to level flight after a disturbance while still allowing the elevator ample control authority over pitch. The mass distribution was determined from a CAD model of the aircraft. XFLR5, an open-source aerodynamic analysis software, was then used to determine the flight characteristics with the center of mass in the appropriate locations for each mission. It was found that the neutral point was 6.85 inches behind the leading edge of the wing. Combining this with mass distribution data leads to the static margins as shown in **Table 4.3.2**. They are at the higher end of the optimal range, driven by the aircraft design that has many major components in front of the wing. The large elevator will help to mitigate any potential control issues that could arise from these static margins. Furthermore, the stability derivatives were calculated in XFLR5, and are also in **Table 4.3.2**. The aerodynamic performance curves for the three missions are shown in **Figure 4.3.2**. The peak of the C_L/C_D curves occurs approximately at the angle of attack where the C_m is zero, indicating an aircraft balanced well for efficient flight.

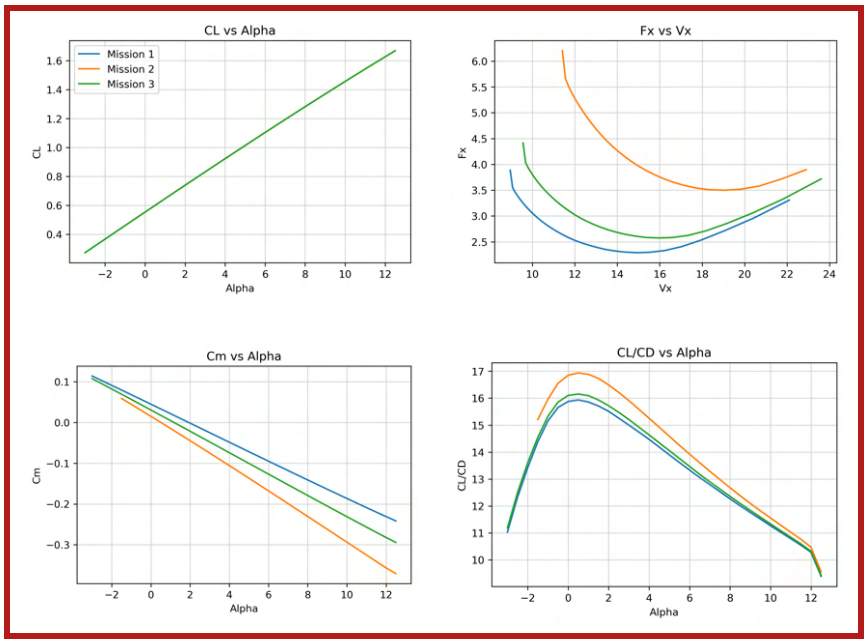

Figure 4.3.2: Aircraft aerodynamic performance

	Mass Properties		Stability Derivatives		
	Mass (lb)	**Static Margin (%)**	$\delta C_m/\delta\alpha$	$\delta C_l/\delta\beta$	$\delta C_n/\delta\beta$
Mission 1	7.45	-23.7	-1.49	-0.06	0.19
Mission 2	12.35	-29.40	-1.84	-0.07	0.20
Mission 3	8.27	-26.30	-1.64	-0.07	0.20

Table 4.3.2: Stability derivatives for all missions

4.3.3 Dynamic Stability Characteristics

Mission	Parameter	Longitudinal Modes		Lateral Modes		
		Short-period	Phugoid	Roll Subsidence	Dutch Roll	Spiral Divergence
M1	Natural Frequency (Hz)	1.61	0.13	-	0.87	-
	Time to halve/double/damping ratio	$\zeta = 0.69$	$\zeta = 0.02$	$t_{1/2} = 0.10$	$\zeta = 0.18$	$t_2 = 2.8$
M2	Natural Frequency (Hz)	2.23	0.10	-	.90	-
	Time to halve/double/damping ratio	$\zeta = 0.59$	$\zeta = 0.03$	$t_{1/2} = 0.15$	$\zeta = 0.12$	$t_2 = 4.46$
M3	Natural Frequency (Hz)	1.79	0.12	-	0.92	-
	Time to halve/double/damping ratio	$\zeta = 0.66$	$\zeta = 0.02$	$t_{1/2} = 0.10$	$\zeta = 0.17$	$t_2 = 3.25$

Table 4.3.3: Dynamic stability characteristics

A dynamic stability analysis was conducted in XFLR5 in order to determine the flightworthiness of the aircraft. The full equations of motion of the aircraft were simplified and linearized about the steady flight condition. This allows the response of the aircraft to disturbances in its flight condition to be modeled as the sum of contributions from various modes. Any real world disturbance will excite all modes, so in order for the aircraft to be inherently stable, all modes must be stable. The results of the dynamic stability analysis are shown in **Table 4.3.3**. All the modes are stable except for the spiral divergence. The pilot will need to consider the instability of the spiral mode, as it has a low doubling time for all three missions. This will require careful monitoring and quick reaction times to ensure that the aircraft does not enter an unrecoverable spiral. Additionally, a stabilizing gyroscope is incorporated into the receiver, assisting the pilot in maintaining level flight. With these considerations, the unstable spiral mode was deemed acceptable.

4.3.4 Analysis of Wingtip Devices

Due to the unstable spiral mode discussed in the previous section, the team thought it prudent to increase the aircraft stability by adding vertical surfaces to the design. To reduce the impact of this addition on the drag characteristics of the aircraft, they were included as wingtip devices so that they primarily inhibit induced drag. An analysis of the effects of the winglets was conducted in Ansys Fluent [2]. Plots comparing the CL and the CL/CD of the wings with and without winglets are shown in **Figure 4.3.4**. The inclusion of the winglets have a very minimal impact on the efficiency, especially at higher angles of attack. Additionally, the winglets slightly increase the lift that the wing generates, increasing the lifting capacity of the aircraft. This analysis concluded that the winglets are not detrimental to the aircraft aerodynamics. As such, winglets shown with a selection of streamlines in **Figure 4.3.3** are included in the final design. The chosen design has a six inch span and a 30.00 degree angle from the chord line, as inspired by Whitchomb's winglet design [8].

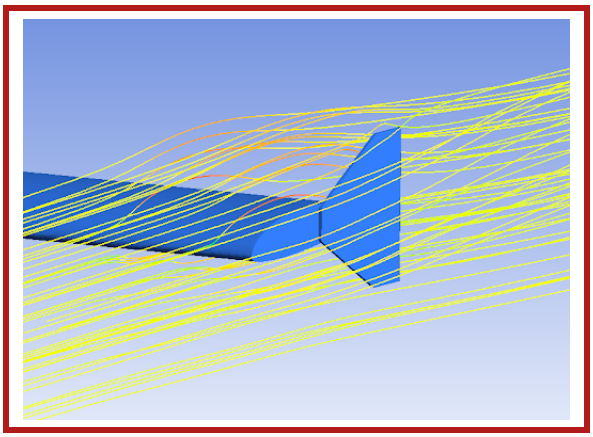

Figure 4.3.3: CFD analysis of streamlines around the winglet

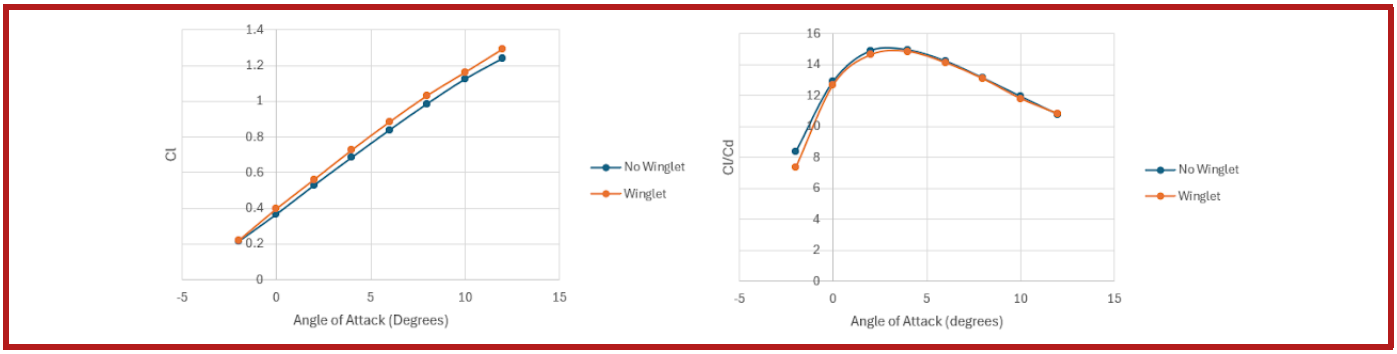

Figure 4.3.4: Simulated aerodynamic data of the wing with and without winglets

4.3.5 Turning Performance

An important aspect of successfully completing all of the missions is the ability of the aircraft to turn quickly and tightly. From a structural analysis, it was determined that a maximum load factor of 1.5 was acceptable to ensure the structural integrity of the aircraft. The maximum rotation rate can be calculated by **Equation 12**, where n_{zs} is the load factor. From the maximum rotation rate the minimum turning radius can be calculated by **Equation 13**. The expected rotation rates for each mission are summarized in **Table 4.3.4**.

$$\Omega_{max} = \frac{g}{V_{stall}} \sqrt{n_{zs} - \frac{1}{n_{zs}}} \tag{12}$$

$$\frac{1}{R_{min}} = \frac{\Omega_{max}}{\sqrt{n_{zs} V_{stall}}} \tag{13}$$

Over the course of a lap, the aircraft will be required to turn 720 degrees, leading to an average turning time of approximately 13.74 s. The average turning radius for the aircraft is 14.02 ft. This is quite small compared to the approximately 1,000 ft length of the competition pattern, allowing the aircraft to efficiently turn around without substantially increasing the distance flown.

Mission	v_{stall} (ft/s)	Ω_{max} (degrees/s)	R_{min} (ft)
M1	29.00	58.17	11.75
M2	36.96	45.65	16.91
M3	31.63	53.34	13.39

Table 4.3.4: Rotation analysis data

4.3.6 Fuselage Aerodynamics

Over the course of the design process, the fuselage shape went through several iterations. An important consideration in the final geometry was the aerodynamic characteristics. Given its position at the front of the aircraft, minimizing the drag created by the shape was a key concern. Two different versions of the fuselage were modeled in ANSYS Fluent to determine their coefficients of drag. Contours of the air velocity over the two potential designs are shown in **Figure 4.3.5**. The initial design had a coefficient of drag of 1.18×10^{-3}, and the second design had a coefficient of drag of 1.38×10^{-3}. Although the drag is 16% higher for geometry on the final design, this increase was necessitated by internal space requirements for the fuselage. The impact of this design change was determined

to be minimal, as the predicted drag coefficient for the wing, as discussed in **Section 4.3.4**, is 1.72×10^{-2}. As such, the increased size of the fuselage only increased the total drag coefficient by approximately 1.00%.

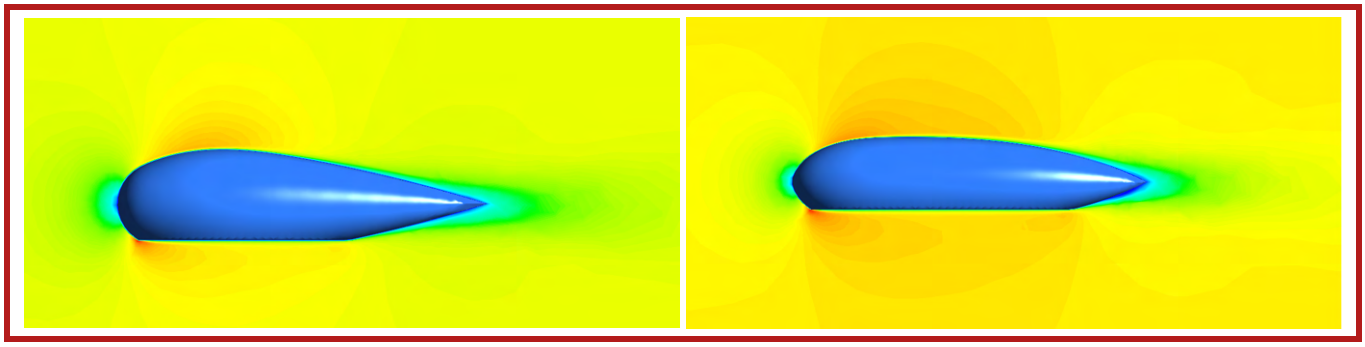

Figure 4.3.5: CFD analysis of initial fuselage design (left) and final design (right)

4.3.7 Aircraft Drag Analysis

The expected drag on the aircraft comes from several sources, principally induced drag and parasitic drag. The induced drag comes from the generation of lift and thus varies between the missions as the mass of the aircraft changes. The parasitic drag comes from the shape of the aircraft, with major contributing factors being the fuselage and the external fuel tanks. The expected drag coefficients for each mission are included in **Table 4.3.5**. The induced drag was calculated in XFLR5 using the angle of attack where the aircraft is balanced. Additionally, the parasitic drag was determined from the CFD analysis of the fuselage and of the wing, in addition to assuming that the external fuel tanks are cylinders. Finally, the parasitic drag coefficient was increased by 30% to account for unmodeled components such as the empennage and the X-1 test vehicle.

Coefficient	M1	M2	M3
C_d	0.068	0.056	0.063
$C_{d,\ induced}$	0.047	0.035	0.042
$C_{d,\ parasitic}$	0.021	0.021	0.021

Table 4.3.5: Expected drag coefficients

4.3.8 Analysis Uncertainties

The analysis discussed in the previous sections includes many simplifications and assumptions. There are factors that will affect the aircraft in flight that were not included in the analysis, such as the presence of the pylons and the test vehicle along with weather conditions. Additionally, the trailing edge of the airfoil had to be modified slightly from the original shape in order to ensure manufacturability, and this modification is not accounted for in the XFLR5 analysis.

In order to determine the handling qualities of the aircraft as well as its performance in adverse weather conditions, a variety of flight tests are required. Although flight testing is needed for full validation, the analysis has yielded accurate general characteristics, confirming the design's viability.

5 Detailed Design

The following section describes the finalized design of Yeägerflug in detail from a subsystem level and includes a center of gravity analysis, aircraft performance, mission performance, and a CAD drawing package.

5.1 Subsystem Design

In the detailed design phase, the major aircraft subsystems were put in CAD using SOLIDWORKS. Each component was created as an individual part, which can then be used to generate an assembly of the entire aircraft, which serves as a reference and as a blueprint for prototyping. For ease of communication across the subteams, a set of CAD conventions was established. The coordinate system of the design has the origin set at the leading edge of the wing, on the plane of symmetry. The axes follow the right hand rule, with the positive x-axis pointed forwards, the positive y-axis pointed along the right wing, and the positive z-axis pointed downwards. Additionally, a standardized set of colors are used. Balsa wood components are colored grey, hardwood components red, and components of other materials have that material's default SOLIDWORKS appearance.

5.1.1 Fuselage Detailed Design

The aircraft fuselage is designed to balance mass and strength while also taking into consideration the volume needed to house components such as the battery, the accompanying wiring, and the X-1 test vehicle launch mechanism. The fuselage is a thin carbon fiber structure that contains a cut-out in the shape of the airfoil so that it can be secured to the wing. To prevent the fuselage from shifting on the wing, two bolts pass through the top of the fuselage and the wing spar to the bottom of the fuselage. The nose of the fuselage is an aerodynamic parabolic shape to help reduce the drag it creates. The bottom of the fuselage is a 14.00 in flat portion for electronic and glider components to rest on. The X-1 test vehicle launch mechanism is glued to the flat surface on the bottom of the fuselage, and the components needed by the propulsion subteam are mounted above it on a 3D-printed platform. A slot in the bottom of the fuselage allows the test vehicle launch mechanism to move during test vehicle launch. The slot is covered with a permanently attached carbon fiber bomb bay door, which will be closed during M1 and open during M2 and M3. A 6.00 in by 4.50 in hatch cut in the top of the fuselage allows access to the parts inside, and is secured to the fuselage using a bolted hinge. The dimensions of the fuselage are 18.79 in by 4.76 in by 3.84 in. It is 0.05 in thick and weighs 0.35 lb. The CAD renderings in **Figure 5.1.1** shows the shape of the fuselage design.

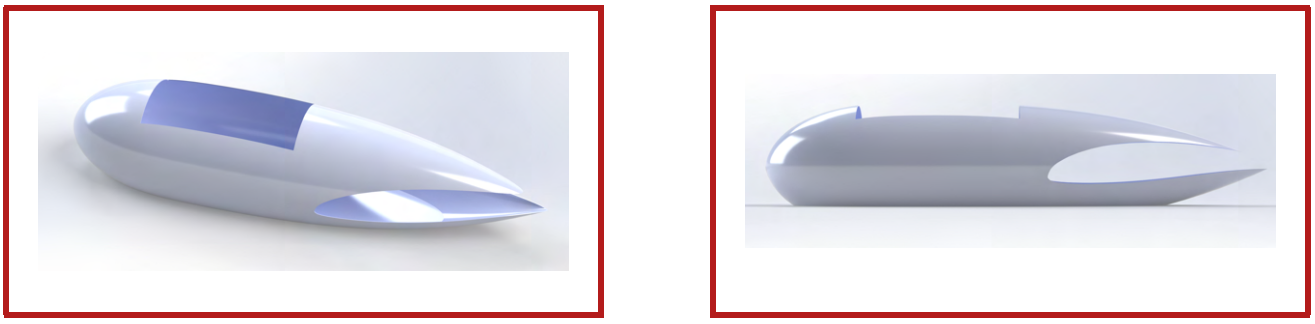

Figure 5.1.1: Isometric view (left) and side view (right) of the fuselage CAD

5.1.2 Landing Gear Detailed Design

Landing Gear and Integration The landing gear is set in a taildragger configuration, with two fixed main gear just ahead of the wing and two small fixed wheels at the rear of the aircraft. The configuration results in a 13.75° angle between the chord line and the ground. In order to support the large wingspan and wing-mounted payloads, the main gear are mounted such that the wheels nearly line up with the payloads on the y axis of the aircraft. Each main gear assembly consists of a carbon fiber curved strut with a 3.54 in diameter rubber wheel attached via an axle to one end. The top of each strut is a flat section through which four holes are drilled for integration. The gear will be integrated directly into the tail spars with 1/4 in bolts and a 3D-printed integration piece. The 3D-printed integration piece is necessary to increase the ground clearance to accommodate the propellers, X-1 test vehicle, and external payloads, along with securing the gear against shear and torsional loading during landing.

Fuel Tanks Each pylon consists of a curved carbon fiber plate encompassing the top half of a standard Gatorade bottle, which serves as the fuel tank. Carbon fiber was selected for this structure due to its high strength-to-weight ratio. Nylon straps epoxied to the carbon fiber wrap around the bottle and buckle tightly to hold it in place. One pylon will be mounted on each wing, outboard of the propellers. The top of the carbon fiber structure has a rectangular extrusion with two holes for 3/16 in diameter clevis pins. The clevis pins extend upward through the holes in the integration piece. This configuration distributes the load on the clevis pin head and ensures that the heads do not interfere with the bottle's fit in the carbon fiber curvature. The pins extend up two inches, inserting into holes drilled in the wing spar. The clevis pins are secured in place using a ¾ in long cotter pin. These pins support the weight of the pylons and fuel tanks, transferring the load to the wing spar. 3D-printed spacers slide over the clevis pins and rest in between the wing spar and carbon fiber plate in order to prevent movement in the z direction. A combination of high-friction material and 3D-printed tabs are attached to the straps in order to prevent bottle motion in the x direction.

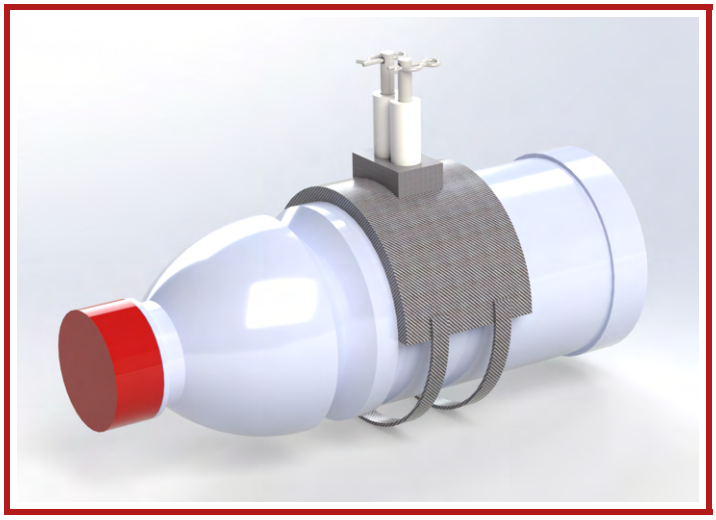

Figure 5.1.2: Fuel tank/pylon integration CAD

5.1.3 Wing Detailed Design

The wing configuration is a non-tapered mid-wing with no dihedral, and it only has ailerons for control surfaces. Due to the fuselage's parabolic shape, a mid-wing allows the fuselage to wrap around the wings and maintain its shape.

Although the mid-wing creates more load in the middle of the fuselage, where it is structurally weakest, it is balanced by improved flight speed, maneuverability, and stability. Other configurations such as flying V and flying wing were ultimately ruled out as they had reduced stability and control performance along with difficulty in manufacturing [9]. A dihedral is made unnecessary by the stability of the mid-wing configuration. Lastly, given the unlimited take-off field length, flaps are unnecessary and their absence leaves more room for the fuel tanks and test vehicle integration. Detailed dimensions are located in **Table 5.1.1**, which were determined by the sizing process described in **Section 3.2**.

The design for the full wing was modeled in SOLIDWORKS, which is shown in **Figure 5.1.3**. The full wing is composed of 14 $\frac{1}{8}$ inch balsa ribs and 9 $\frac{1}{8}$ inch hardwood ribs. The rib material was chosen to balance weight and structural integrity. The hardwood ribs either bear the servo load, or are the innermost or outermost ribs and therefore provide structural integrity to the wing root and tips. The stringers around the ribs provide structure and attachment points for the MonoKote. A hardwood rear comb provides structure and attachment points for the control surfaces. The sharp, curved trailing edge of the FX 63-137 airfoil is replaced by a triangular balsa block in order to facilitate manufacturing while still resembling the original airfoil shape. A single continuous carbon fiber spar runs through the wing to provide bearing the flight loads and facilitates integration with the pylons, fuselage and tail spars. The wing spar intersects the tail spars perpendicularly, which extend to the tail on one side and the motor-propeller system on the other.

The ailerons are also constructed of balsa and hardwood ribs, with a hardwood comb. A FrSky Xact HV5611 servo sits on a plate on the lower surface of the wing for each aileron. Control rods attach the servos to the control horns, which are secured to hardwood plates on the ailerons. Hinge points connect the hardwood combs of the ailerons and the main wing, and balsa blocks are glued onto the inner faces of the wing's rear comb and the ailerons' front comb to help secure the hinges.

Parameter	Value
Airfoil	FX 63-137
Planform Area (in^2)	734.72
Aspect ratio	6.48
Wingspan (in)	69.00
Chord (in)	10.65
Aileron Chord Percentage	30.00 %
Aileron Wingspan Percentage	59.75 %
Estimated mass (lbs)	1.61

Table 5.1.1: Wing dimensions

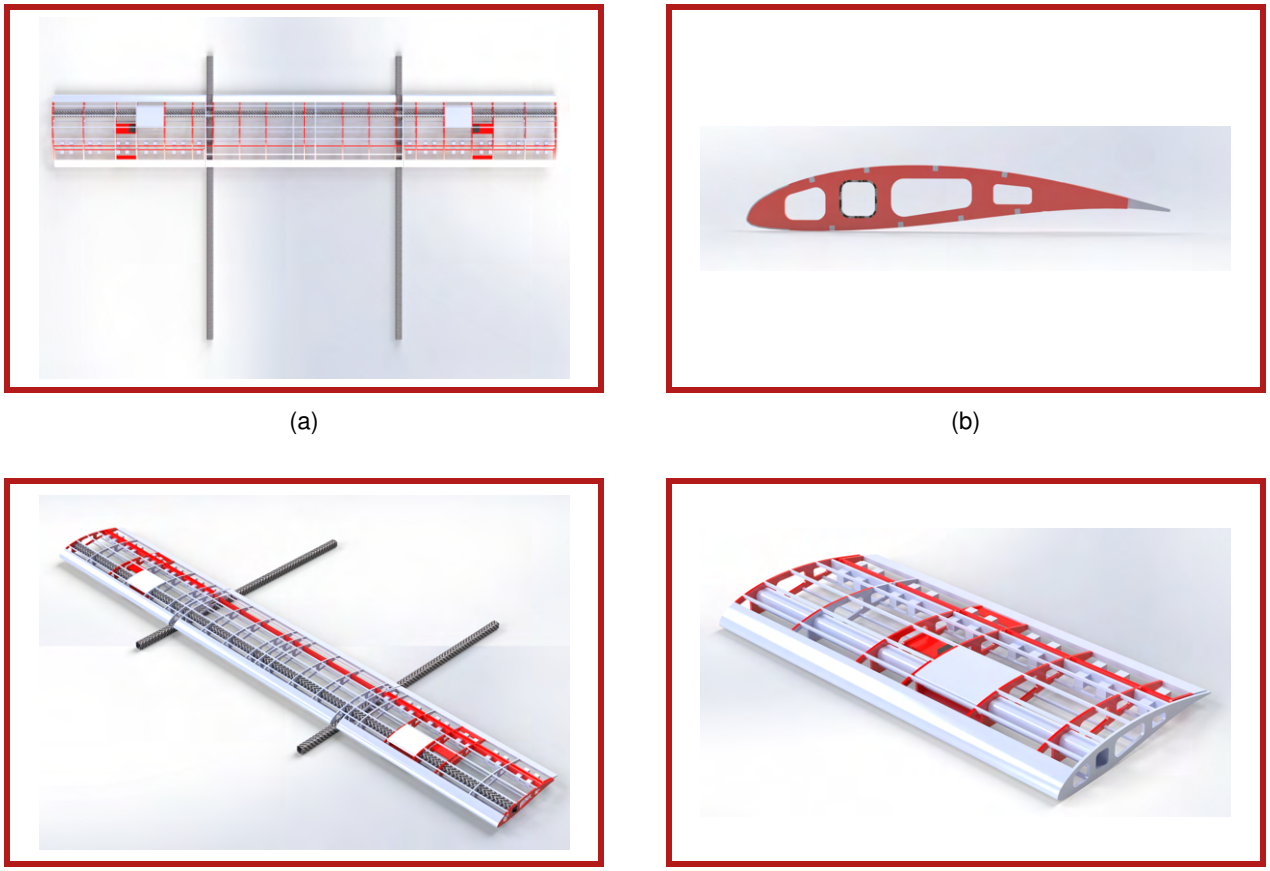

(a) (b)

(c) (d)

Figure 5.1.3: Top view (a), side view (b), isometric view (c), and close view of the right wing (d)

5.1.4 Empennage Detailed Design

The dimensions of the stabilizers were determined using the sizing script described in **Section 4.2.2**. The widths of the airfoil ribs for the stabilizers are $\frac{1}{8}$ in, balancing structural integrity and weight. The stringers lining the spans of all the stabilizers are made of balsa, as their main purpose is to provide a geometric outline for the MonoKote to cover. The leading edges of the stabilizers are hardwood to prevent warping from the pressure exerted by the MonoKote. The tail is connected to two carbon fiber spars that go perpendicularly through the horizontal stabilizer. The spars pass through the front and rear combs and between the two outermost ribs of the horizontal stabilizer.

The trailing edges of the control surfaces are triangular balsa pieces. The elevator is a single surface that extends the entirety of the span of the horizontal stabilizer to create a more consistent elevator movement. Balsa blocks are placed on the inner faces of the rear comb of the stabilizers, as well as the inner faces of the control surfaces to give the hinge pins a depth to hold onto, allowing the surfaces to be attached more securely. Both the vertical stabilizers and the horizontal stabilizer use a FrSky Xact HV5611 servo to actuate their control surfaces. The CAD rendering of the empennage is shown below in **Figure 5.1.4**.

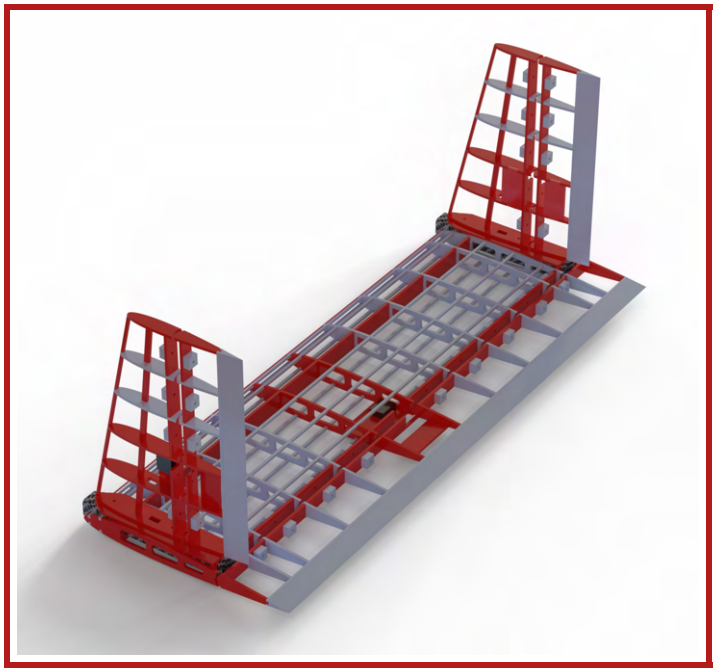

Figure 5.1.4: Empennage CAD

5.1.5 Empennage Integration Detailed Design

The integration of the empennage includes attaching the horizontal and vertical stabilizers to the tail spars. For the integration of the horizontal stabilizer, the tail spars are inserted into the perpendicular combs towards the front and rear of the horizontal stabilizer. This ensures that the horizontal stabilizer does not shift along the y or z axes. The height of the combs at these specific places are adjusted to allow a minimum thickness of $\frac{1}{8}$ in between the spar holes and the outer edge of the comb. For the vertical stabilizers, the bottom-most rib plates are laid onto flat plates at the edges of the horizontal stabilizer, where they are each secured using two bolts that extend through the tail spars. These bolts are situated towards the front and rear of the bottom ribs to and prevent the vertical and horizontal stabilizers from shifting in the x direction. The CAD rendering of the empennage integration is shown below in **Figure 5.1.5**.

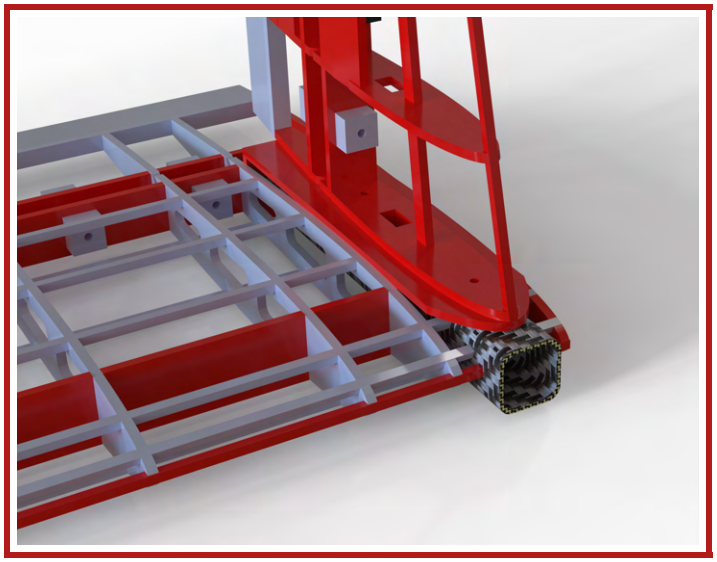

Figure 5.1.5: Empennage integration detailed design

5.1.6 Wing Payload Integration Detailed Design

Holes in the wing spar provide an attachment point for the clevis pins which support the pylons. On each side of the wing, a hardwood plate on the lower surface of the wings provides additional support for the clevis pins. On the wing's upper surface, a 3D-printed hatch is attached to the ribs, which allows access to the cotter pins so that the pylons and fuel tanks are easily removable. A CAD model of the hatch is shown below in **Figure 5.1.6**.

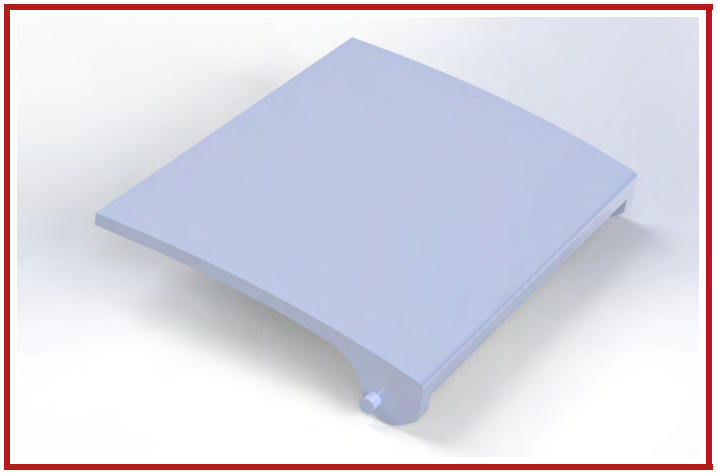

Figure 5.1.6: Hatch CAD

5.1.7 Propulsion Detailed Design

Through all missions, a single Tattu 4500mAh 6s LiPo battery provides propulsive power. The power runs through a 100A fuse, before splitting between two Cobra 60A electronic speed controllers (ESCs). The ESCs feed the power to their respective Cobra CM-4515/18 motors, each mounted on the wings. Each motor has a 14 in x 10 in APC

propeller, and is configured so that the inboard side of each propeller rotates upwards. The counter rotation prevents the leftward rolling and p-factor tendencies that would come from both propellers spinning in the same direction, helping ensure stability. The propulsion system is accompanied by an Eagle A3 Super 4 Airplane Gyroscope that assists the pilot in preventing the aircraft from rolling into an unstable position. All control surfaces are actuated by rSky Xact HV5611 servos connected to a Spektrum AR630 6 Channel Receiver. The receiver is controlled by a Spektrum DX-8e transmitter. The receiver itself is powered separately by a Bancroft 320mAh 2S LiFePO4 Battery. A detailed wiring diagram is illustrated in **Figure 5.1.7**

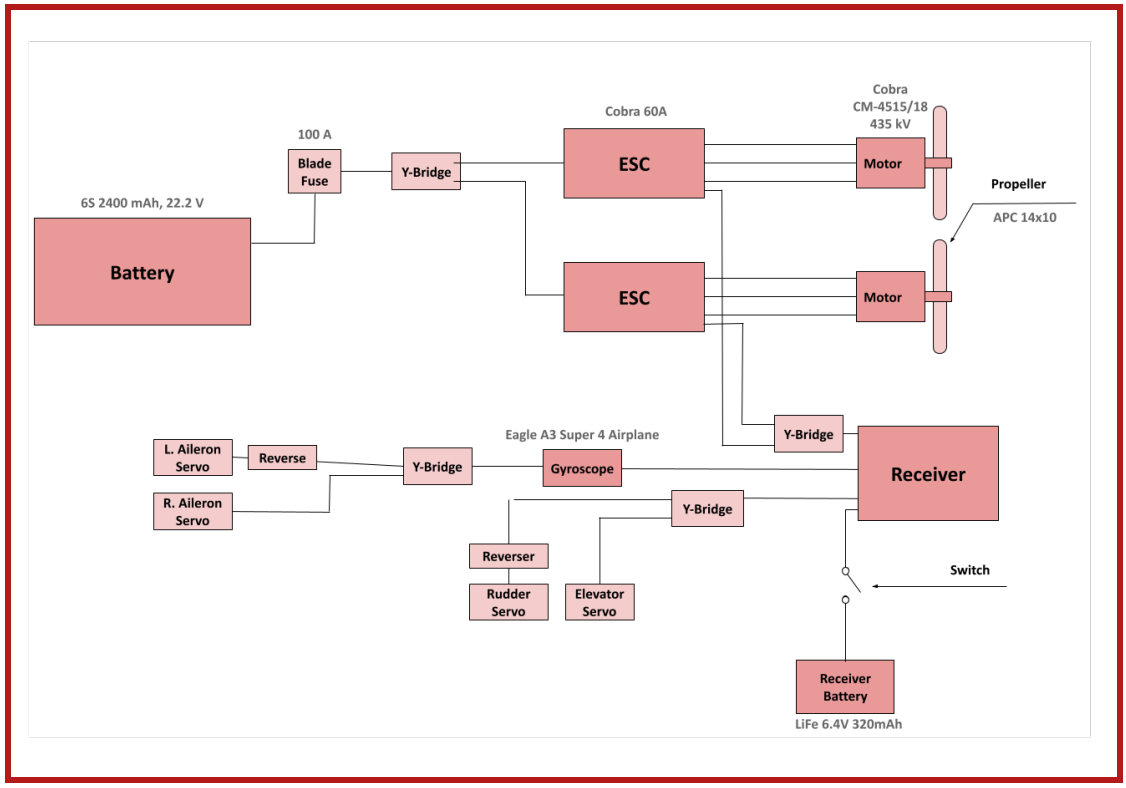

Figure 5.1.7: Wiring diagram of the propulsion system

5.1.8 Electronics Integration Detailed Design

The electronics integration piece is a 3D-printed structure designed to house the LiPo battery, servo battery, and receiver to maintain wiring configurations within the fuselage. The primary component featured in **Figure 5.1.8** measures 2.60 in x 6.40 in, with its bottom partially curved to align with the fuselage's shape. Velcro secures the electronics to the integration piece and allows for easy manipulation during ground mission and staging. The battery is oriented towards the nose, allowing the fuse to rest on top of it. The wires from the battery branch into two ESCs at the base of the wings. Behind the battery in the rear of the integration piece, the receiver and servo battery are secured with velcro, facilitating organized wiring. Another consideration was designing the integration piece around the internal test vehicle launch mechanism. Using the flat surface established by the launch mechanism underneath, velcro secures the bottom of the integration piece to the mechanism to stabilize the components within the fuselage.

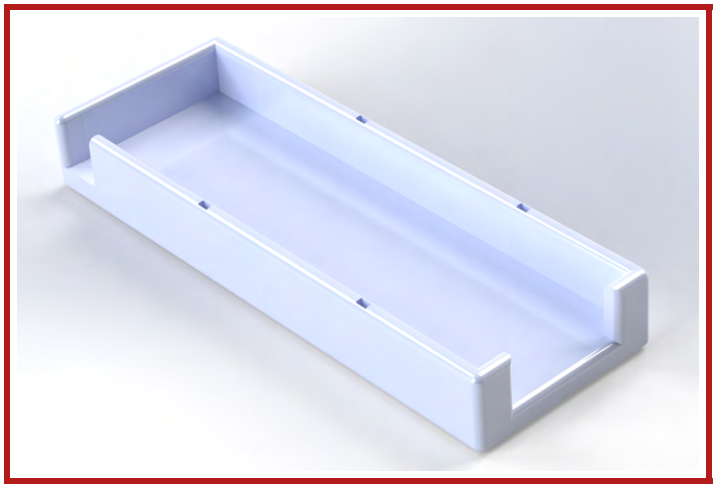

Figure 5.1.8: Electronics integration component

5.1.9 Motor Integration Detailed Design

The motors are mounted ahead of the leading edge of the wing, on extensions of the tail spars. Integration pieces, 3D-printed out of Onyx for structural rigidity, are bolted to the end of the spar. Sized to withstand thrust, torque, and weight estimates, their radii are also minimally larger than that of the motors, to allow for metal cross-mounts. The resulting CAD of the motor mount integration piece is shown in **Figure 5.1.9**. The two cross-mounts, machined in-house out of steel, are sized to match the motor and integration piece screw holes exhibited in **Figure 5.1.10**. This custom configuration allows the motor to be removed from the aircraft without disassembling the entire integration piece, a problem encountered with commercially available cross-mounts.

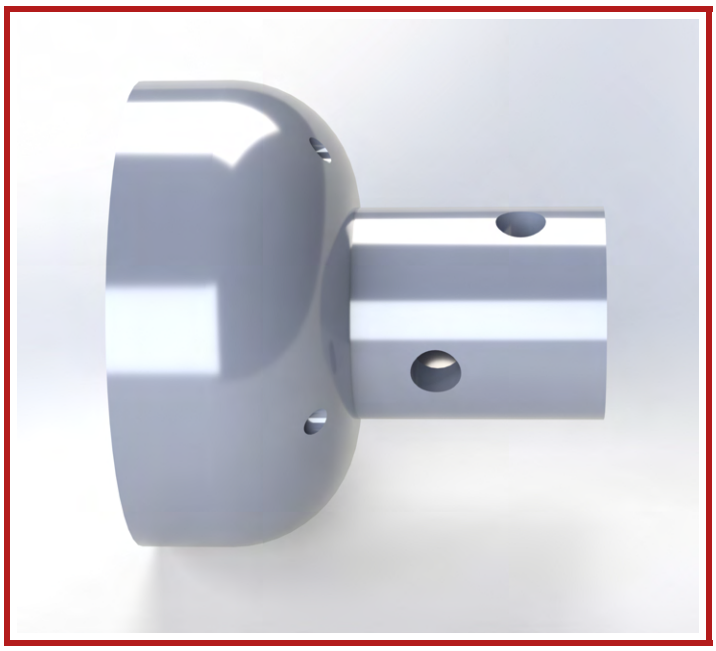

Figure 5.1.9: CAD of motor mount integration piece

Figure 5.1.10: Steel motor cross-mount

To determine motor placements, ANSYS simulations based on CAD models of potential propellers were used to analyze the effects of propeller positions on lift surface efficiencies at cruise speeds. aerodynamic studies conducted by professor Veldhuis [12], provided consideration of the outward, forward, and vertical distances and incidence angles from the fuselage. Ultimately, the motors are placed 7.6 in forward of the leading edge, and at an incidence angle of two degrees.

5.1.10 Test Vehicle Detailed Design

X-1 Test Vehicle Structure The X-1 test vehicle structure shown in **Figure 5.1.11** is inspired by the geometry of a standard glider. This includes a high aspect ratio wing to reduce drag and increase the glide ratio, as well as a blended fuselage/empennage design. Due to the limited performance requirements imposed on the test vehicle by the rules, major dimensions were simply assigned based on this general philosophy and the geometric constraints of the full aircraft. For example, the wingspan of the test vehicle is 18.00 in, to maximize the aspect ratio while still fitting between landing gear assemblies. Additionally, the test vehicle's fuselage dimensions are determined by the size of the electronics package that must fit within the interior space of the vehicle's fuselage. Furthermore, the wings employ the Eppler 393 airfoil. This airfoil has a high lift-to-drag ratio, improving the vehicle's glide performance.

The physical structure of the test vehicle consists of six foam pieces created by slicing the CAD model six times perpendicular to the y-axis. This produces two dimensional profiles that can then be cut out of foam sheets. The individual slices are glued together to create the whole fuselage structure. Rectangular cutouts are made in the two innermost side profiles so that when they are put together, a hollow space exists for the electronics to be housed in. The vertical stabilizer is designed such that it can be cut out of the same foam sheet as the center fuselage piece, drawing on the blended empennage designs of many common gliders. The wing and horizontal stabilizer are fabricated separately to ensure that they have the proper airfoil profiles. With the electronics installed, the test vehicle

has a mass of 0.49 lb.

Figure 5.1.11: X-1 test vehicle CAD

X-1 Test Vehicle Control Surfaces The test vehicle wing is equipped with elevons to control both pitch and roll simultaneously. This choice of wing control surface allows reliable control of the aircraft within the limited space available. The control surfaces consist of triangular balsa pieces hinged to the foam wing. FrSky Xact HV5611 servos control the motion of the balsa edge via control rods and clamps. The choice of elevons also removes the need to install elevators on the tail, simplifying the design and helping keep the test vehicle balanced.

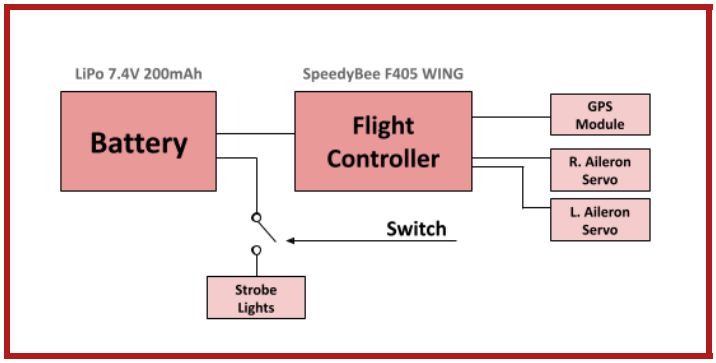

Figure 5.1.12: X-1 test vehicle wiring diagram

X-1 Vehicle Electronics Detailed Design A 7.4V 200mAh 30C LiPo battery powers the X-1 test vehicle's electronics. The batteries, flight controller, and GPS module are housed in the test vehicle's fuselage. Servos and strobe lights are located on the wing and tail of the test vehicle. Illustrated in **Figure 5.1.12**, The flight controller is the SpeedyBee F405 WING, which runs on Ardupilot software and uses a GPS module to determine the X-1 test vehicle's location. The single battery connects to the flight controller and servos, while branching off to a separate circuit that connects to the strobe lights. This additional circuit features a magnetic switch that turns on the strobe lights once the test vehicle disconnects from the aircraft's fuselage. The lights are positioned downwards, ensuring that light can be seen from multiple angles on the ground and from at least 400 ft away.

The SpeedyBee F405 WING flight controller was chosen because of its low weight and simple setup. Using Ardupilot's Mission Planner software [3], a course is established for the X-1 test vehicle to follow. This course involves

waypoints for the test vehicle to complete a 180° turn, as well as setting a return-to-home point above the landing zone. From release, the flight controller directs the test vehicle along this course and lands it safely in the designated area.

Launch Mechanism When the X-1 test vehicle launch signal is sent to the radio receiver, a servo and the attached test vehicle launch arm rotate 10° downwards. The swivelling launch arm has a T-shaped internal slot. When the launch arm rotates downwards, the two mounting screws at the top of the test vehicle slide along this T-shaped rail, launching the test vehicle into a smooth descent. When retracted, the launch arm sits slightly above the horizontal. The geometry of the launch arm, test vehicle mounting screws, and the slot in the fuselage floor prevent the test vehicle from moving backwards in flight until it is released.

A slot in the fuselage floor allows the launch arm to move below the fuselage when the mechanism is activated. During M1 and the ground mission, hinged CFRP bomb bay doors, permanently attached, will cover the slot; this ensures that no part of the test vehicle launch system is exposed or external to the fuselage. Velcro is used to keep the door in the closed or open position depending on whether the test vehicle is attached or not. The overall dimensions of the X-1 test vehicle launch mechanism are 5.97 in x 2.81 in x 1.00 in.

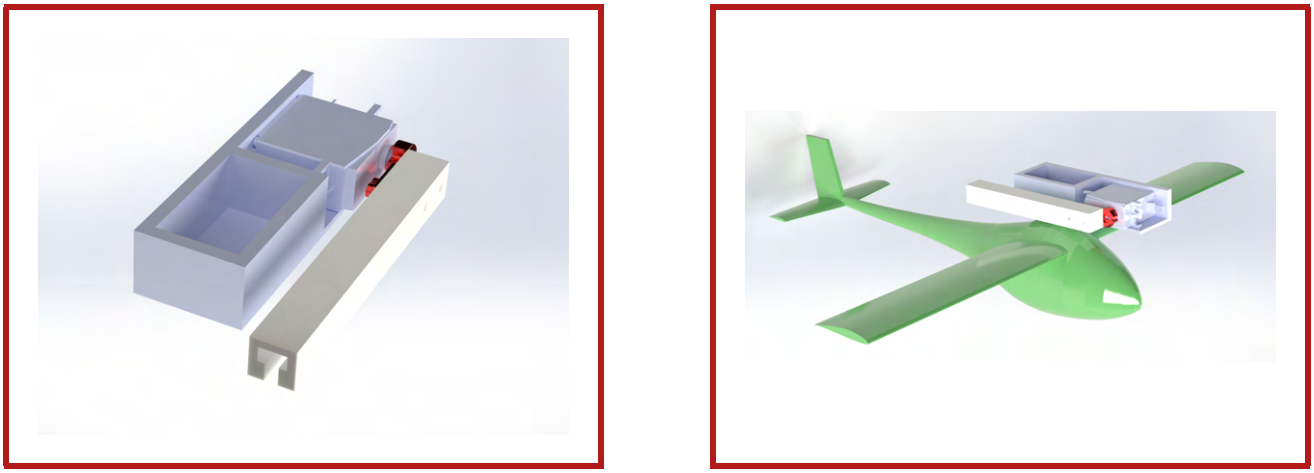

Figure 5.1.13: X-1 test vehicle launch mechanism (left) and integrated launch mechanism with X-1 (right)

5.2 Weight and Balance

The addition of the X-1 vehicle and payloads changes the mass properties between each mission. **Table 5.2.1** summarizes the mass and center of mass for all major components of the aircraft for each mission, which were determined in SOLIDWORKS. ground.

Component	Mass (lbs)	CGx (in)	CGy (in)	CGz (in)
All Missions				
Fuselage	0.66	2.68	0.00	0.00
Main Landing Gear	0.33	0.39	0.00	1.97
Wing	1.98	-4.49	0.00	-0.44
Empennage	1.04	-31.10	0.00	-0.98
Motors	1.28	-6.61	0.00	0.00
Propellers	0.26	-7.61	0.00	0.00
Mission 1				
Total	7.45	-4.45	0.00	-0.20
Mission 2				
X-1 Test Vehicle	0.49	0.00	0.00	2.36
Fuel Tanks	4.41	-3.15	0.00	0.94
Total	12.35	-3.74	0.00	0.94

Table 5.2.1: Weight and balance data

5.3 Aircraft Performance

As the detailed design is derived from the preliminary design, the expected aerodynamics performance and mission performance has not changed. XFLR5 serves as the team's primary software to run lift, drag, and static and dynamic stability simulations. From there, the mission flight speeds and flight times were estimated.**Sections4.3.2** and**4.3.3** explain these performance calculations in detail.**Table 5.3.1** summarizes the expected aircraft performance parameters.

The cruise velocities are used to predict the aircraft performance in each of the competition missions. It is expected that the aircraft will take 1.98 minutes to complete the three laps of M1. The three laps of M2 will take 2.32 minutes to complete. Finally, the aircraft will complete seven laps before the launch of the X-1 test vehicle in M3.

Parameter	M1	M2	M3
Mass (lb)	7.45	12.35	8.27
$C_{L,cruise}$	0.73	0.60	0.67
$C_{D,cruise}$	0.05	0.04	0.04
$C_L/C_{D_{cruise}}$	15.53	14.63	18.61
V_{cruise} (feet/s)	132.64	141.89	93.45

Table 5.3.1: Expected aerodynamic performance

5.4 Drawing Package

The drawing package contains engineering drawings of the aircraft and its major subsystems. Included are 3-View, exploded view, and important individual components. Drawings have parts and major dimensions labeled and materials are assigned. All CAD models are created in SOLIDWORKS.

FRONT VIEW

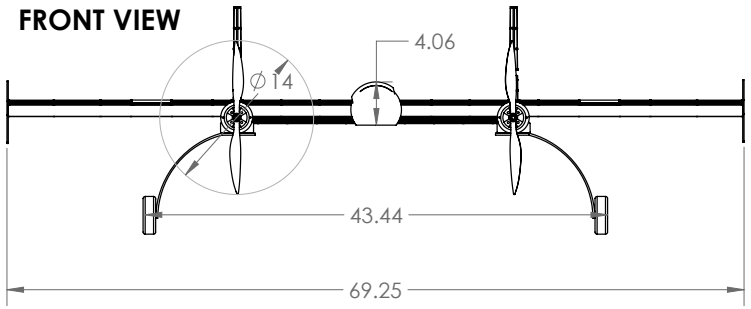

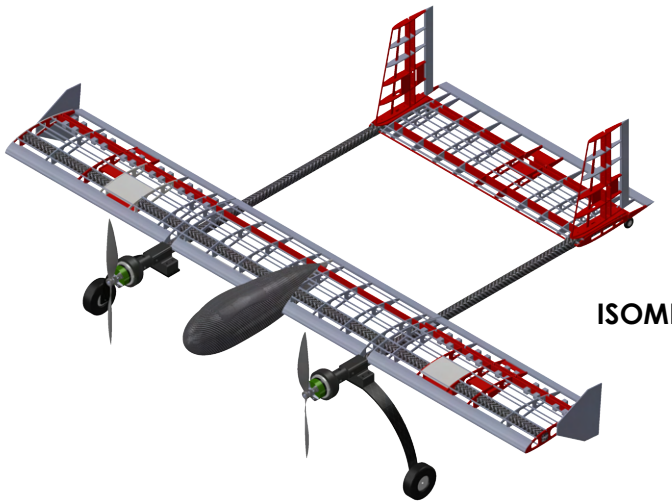

ISOMETRIC VIEW

TOP VIEW

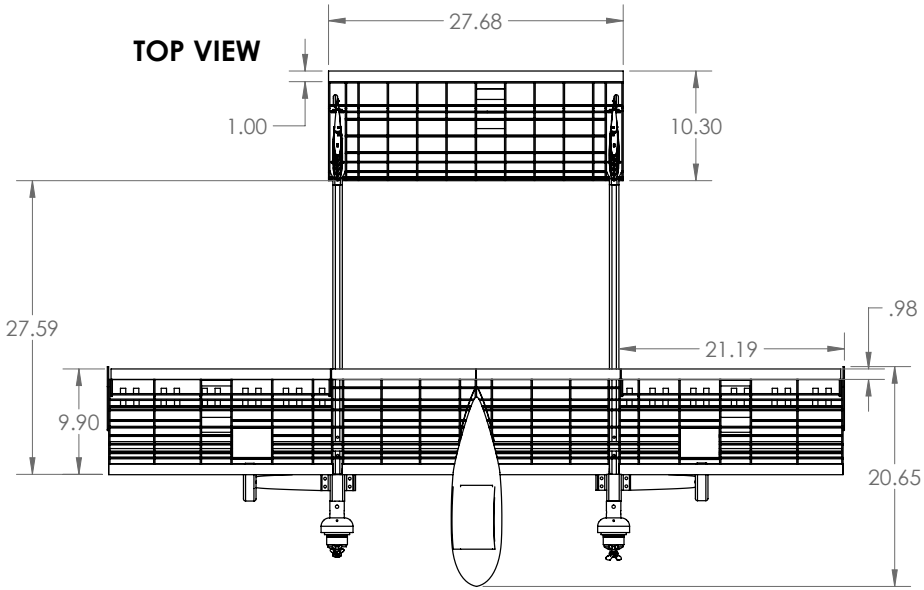

LEFT VIEW

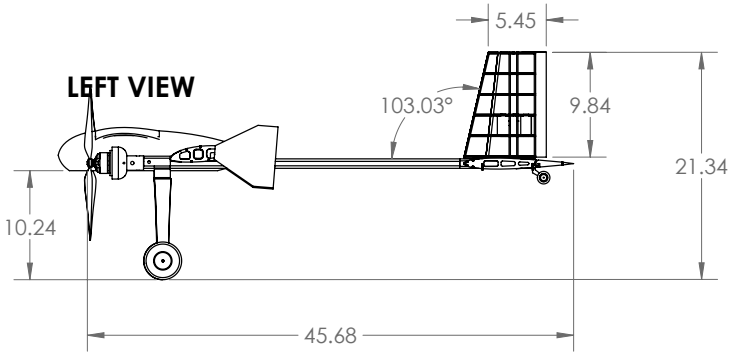

cuDBF	DATE: 02/21/2025	
	Cornell University	
	TITLE: Three-View drawing	
DRAWN BY: Charlotte Huber		
CHECKED BY: Ishan Roy	313 Campus Rd. Ithaca, New York, 14853	A3
M1 WEIGHT: 7.716 lbs	SCALE:1:12	ALL UNITS ARE IMPERIAL [IPS]

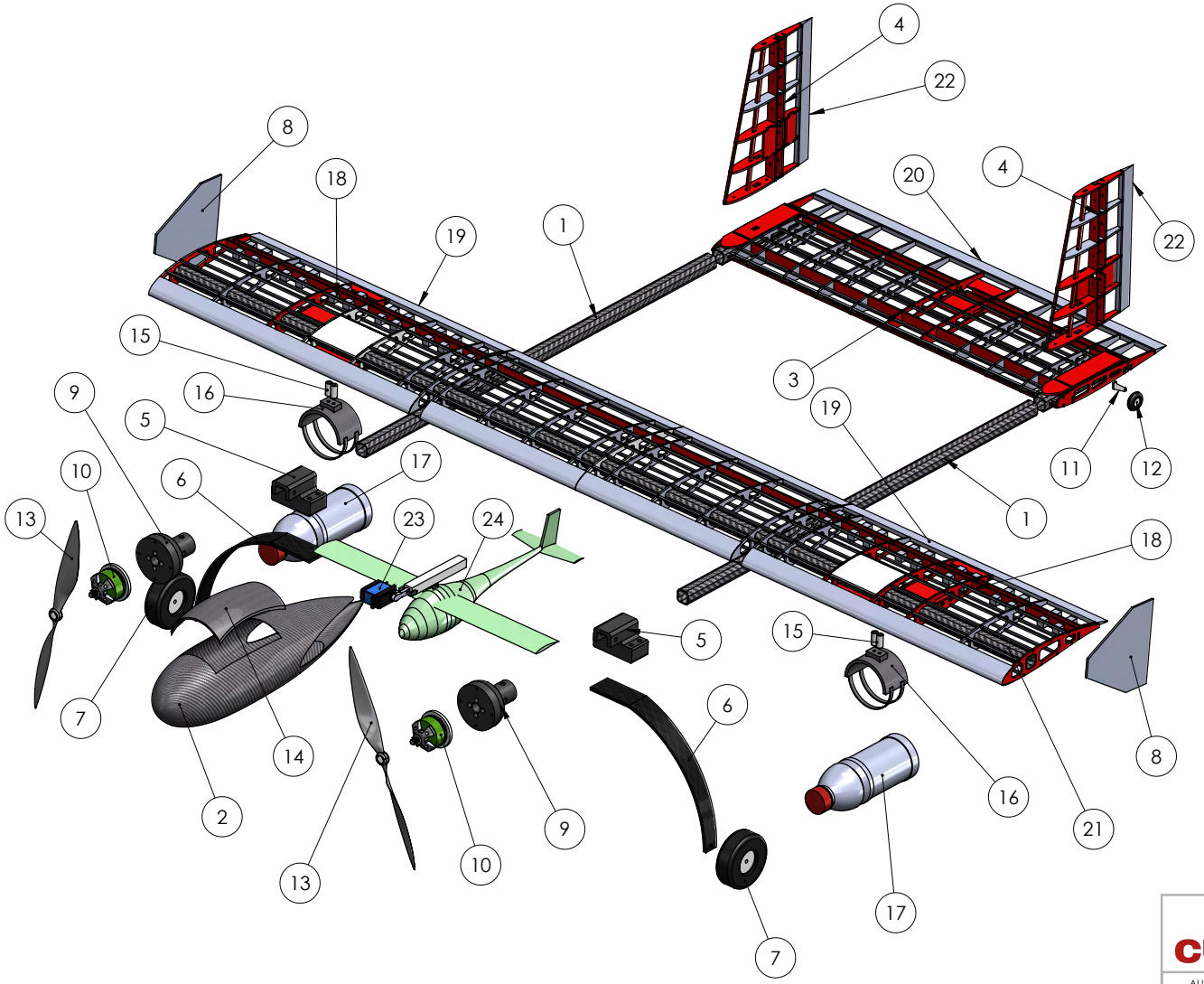

PART NO.	Part Name	Material/Product	QTY.
1	Tail Spar	Carbon Fiber	2
2	Fuselage	Carbon Fiber	1
3	Horizontal Stabilizer	Basswood/Balsa	1
4	Vertical Stabilizer	Basswood/Balsa	2
5	Main Gear Integration	Onyx	2
6	Main Gear Strut	Carbon Fiber	2
7	Main Gear Wheel	Rubber	2
8	Winglet	Balsa	2
9	Motor Mount	Onyx	2
10	Motor	Cobra CM-4515/18	2
11	Tail Gear Strut	ABS	2
12	Tail Gear Wheel	Foam	2
13	Propeller	APC	2
14	Hatch	Carbon Fiber	1
15	Clevis Pin	Steel	4
16	Pylon	Carbon Fiber	2
17	Payload Bottle	Plastic	2
18	Wing	Basswood/Balsa	1
19	Aileron	Basswood/Balsa	2
20	Elevator	Basswood/Balsa	1
21	Wing Spar	Carbon Fiber	1
22	Rudder	Basswood/Balsa	2
23	X-1 Launch System	Servo/ABS	1
24	X-1 Vehicle	EPS Foam	1

cuDBF

DATE: 02/21/2025

Cornell University

TITLE:

Stuctural Arrangement

DRAWN BY:
Raquel Sweet

CHECKED BY:
Ishan Roy

313 Campus Rd. Ithaca, New York, 14853

A3

SCALE:1:7

ALL UNITS ARE IMPERIAL [IPS]

ITEM NO.	Part Name	Material/Product	QTY.
1	Fuselage & Wing Assembly	Foam	1
2	Screw	Steel	2

X-1 GLIDER ISOMETRIC VIEW

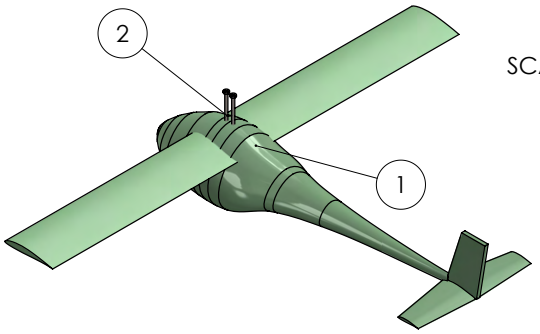

SCALE 1:4

X-1 GLIDER TOP VIEW

SCALE 1:4

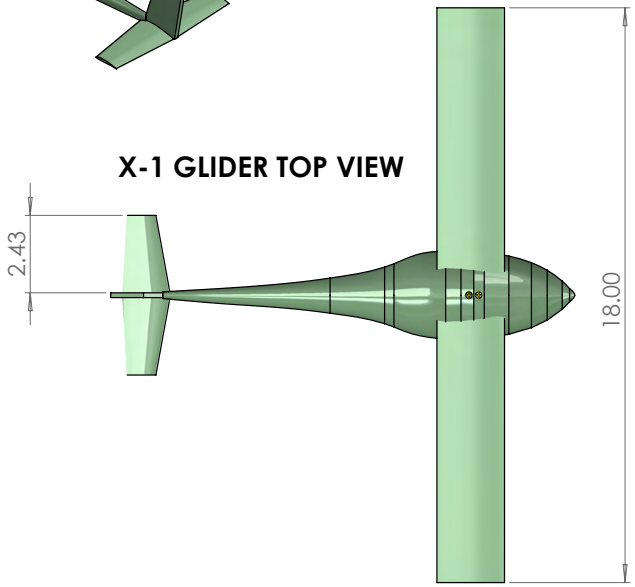

X-1 GLIDER SIDE VIEW

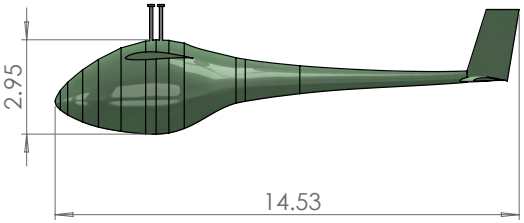

SCALE 1:4

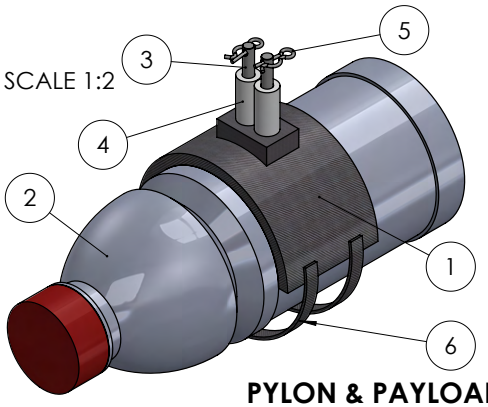

SCALE 1:2

ITEM NO.	Part Name	Material/Product	QTY.
1	Pylon	Carbon Fiber	1
2	Gatorade Bottle	Plastic (PET)	1
3	Clevis Pin	Steel	2
4	Spacer	Aluminum	2
5	Cotter Pin	Steel	2
6	Strap	Nylon	2

PYLON & PAYLOAD ISOMETRIC VIEW

Wing Section

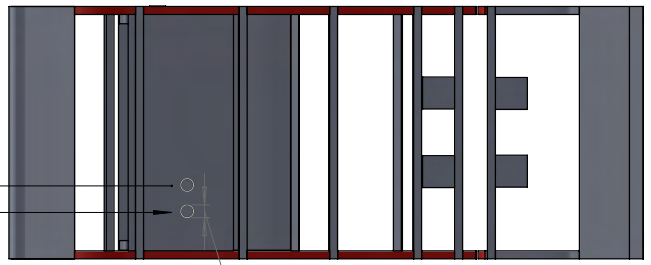

Pylon connection pins and holes

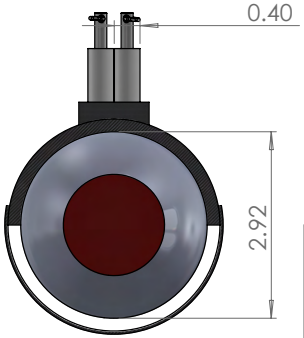

SCALE 1:2

PYLON & PAYLOAD FRONT VIEW

cuDBF	DATE: 02/21/2025	Cornell University
ALL RIGHTS RESERVED BY CORNELL UNIVERSITY DESIGN BUILD FLY	TITLE:	Payload Accomodation
DRAWN BY: Ira Geller		
CHECKED BY: Ishan Roy	313 Campus Rd. Ithaca, New York, 14853	A3
M2 WEIGHT: 12.35 lbs	M3 WEIGHT: 8.27 lbs	ALL UNITS ARE IMPERIAL [IPS]

MISSION 2 & MISSION 3 CONFIGURATION FRONT VIEW

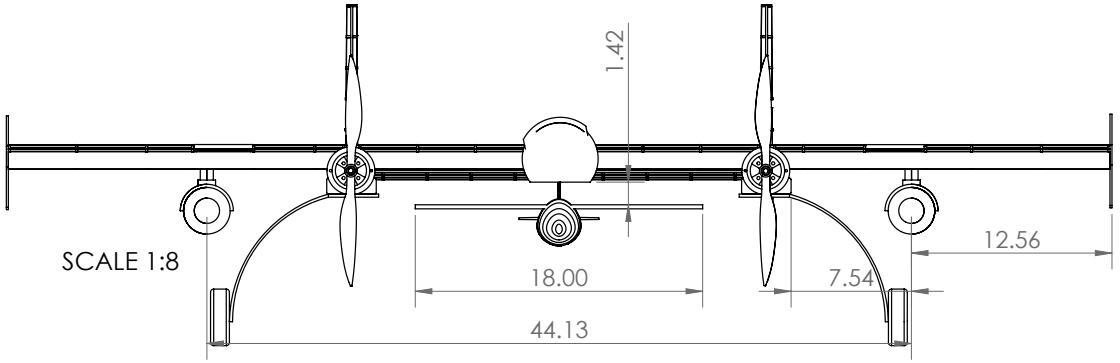

INTEGRATED PAYLOAD ISOMETRIC VIEW

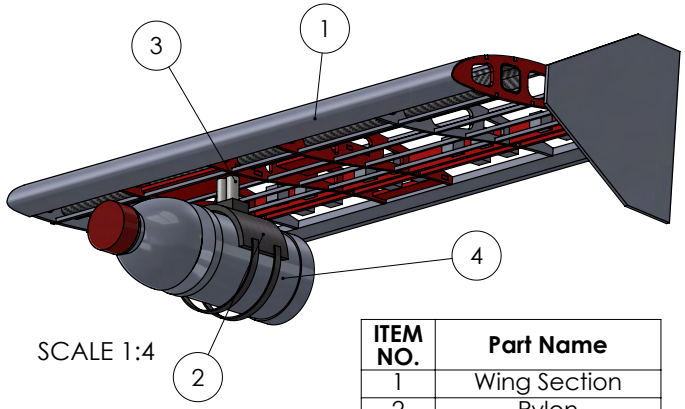

ITEM NO.	Part Name
1	Wing Section
2	Pylon
3	Cotter & Clevis Pin Assembly
4	Bottle

X-1 INTEGRATION AND LAUNCH SYSTEM

Integrated Isometric View

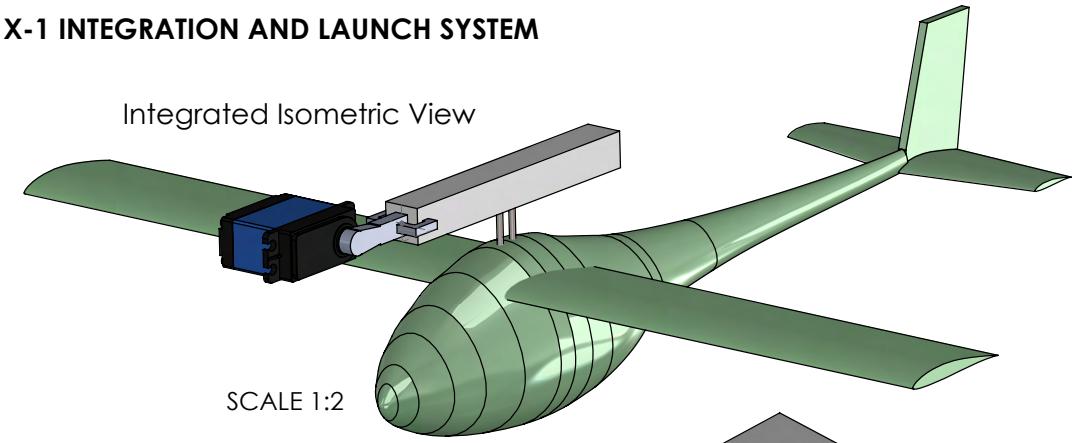

Launch System Isometric View

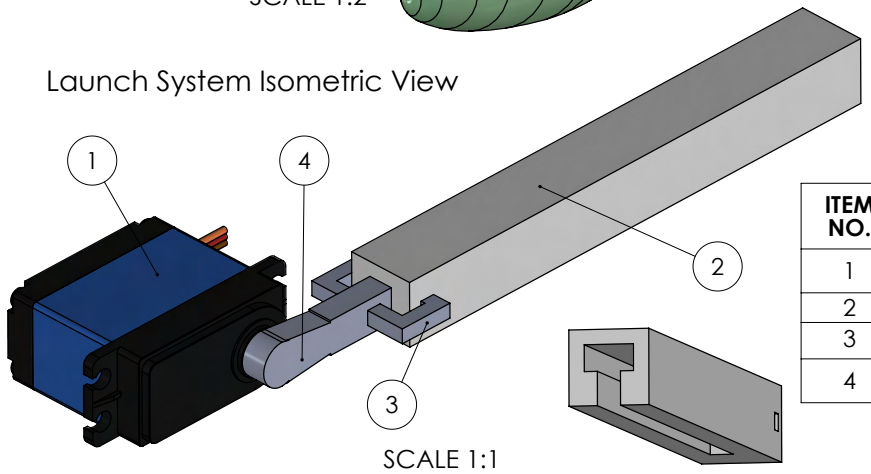

ITEM NO.	Part Name
1	Servo
2	Launch Arm
3	Linkage Arm
4	Servo Arm

Launch Arm Isometric View

PROPULSION ELECTRONICS

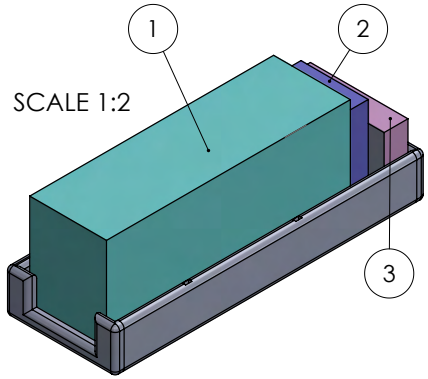

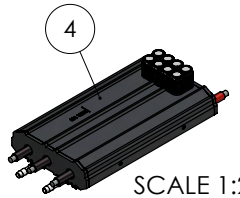

ITEM NO.	Part Name
1	Main Battery
2	Servo Battery
3	Receiver
4	Electronic Speed Controller

cuDBF

DATE: 02/21/2025

Cornell University

TITLE: Systems Overview

DRAWN BY: Ishan Roy

CHECKED BY: Nate Heinzelman

313 Campus Rd. Ithaca, New York, 14853

A3

Battery Weight: 1.43 lbs

ALL UNITS ARE IMPERIAL [IPS]

6 Manufacturing Plan

The aircraft and its components were manufactured using numerous methods including 3D-printing, laser cutting and composite layups. A major component of many design decisions is manufacturability and these parameters need to be considered. These subsections outline the various processes for different components. The fully manufactured aircraft is shown in **Figure 6.2.3** at the end of this section.

6.1 Manufacturing Process

The manufacturing process of the aircraft follows an iteration cycle with four phases: modeling, fabrication, system and subsystem assembly, and analysis and testing, as depicted in **Figure 6.1.1**. After each analysis and testing phase, the cycle was repeated for the next iteration. The manufacturing process is heavily linked with the design and testing processes, with many components being prototyped, tested, and redesigned simultaneously.

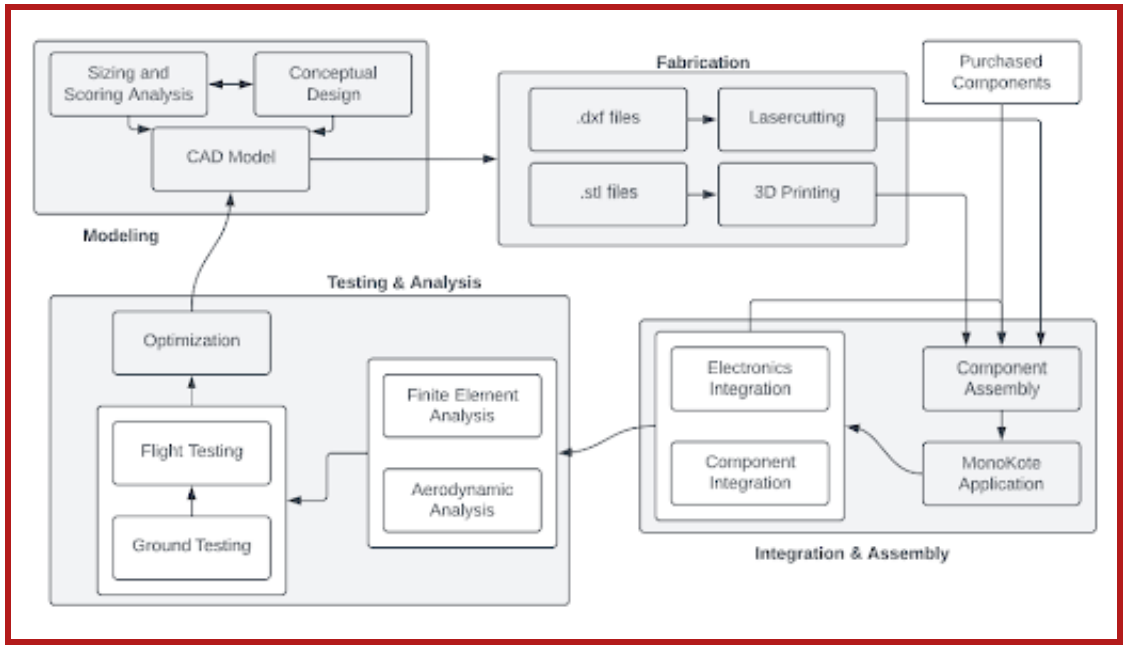

Figure 6.1.1: Manufacturing process flowchart

Modeling began after the competition rules were released. Sizing and scoring analysis for the ground mission were performed using the rules, restrictions, and guidelines to determine which parameters were optimized for the aircraft and mission components. After this optimization along with the initial brainstorming of design specifications, CAD models were developed in SOLIDWORKS to visualize how components will operate and integrate with one another and establish the framework for manufacturing. When fully designed, the models enter the fabrication stage where they are laser cut, 3D-printed, bought commercially, or molded for composite layup.

All manufactured parts, along with externally purchased components are assembled into their respective subsystem components. Materials such as balsa, basswood, resin, carbon fiber, and all electrical components are integrated using epoxy, cyanoacrylate glue (CA), wood glue, heat shrink tubes for wiring, or hardware fasteners including nuts, bolts, and screws. MonoKote, a smooth and continuous film, is used when necessary to tightly encase subsystems/components.If components are not able to integrate smoothly, it becomes necessary to revert back to

the modeling phase and cycle through the manufacturing phase again. By repeating this cycle multiple times, an effective mission-based aircraft is attained.

6.1.1 3D Printing

3D-printing is inexpensive, fast, and allows parts with complicated geometry to be manufactured with ease. 3D-printers used included the Bambu Lab X-1 Carbon for all PLA and ABS components and Markforged Mark Two Onyx 3D-Printer for all onyx components. The printers were used to develop prototyped parts and the final designs for components such as the motor mount and wing hatch. The molds for the composite layup of the fuselage and pylons were 3D-printed using ABS.

6.1.2 Laser Cutting

The majority of the wing and tail were made of balsa and basswood. A laser cutter was used in order to ensure the manufactured parts precisely match the designs. The Epilog Laser Fusion Edge, housed in the Rapid Prototyping Lab at Cornell University, was used to cut wood up to 36 in x 24 in area and ¼ in thick, allowing the team to efficiently print tens of parts at once.

6.1.3 Composite Layups

The fuselage and pylons were manufactured using composite layups, specifically a wet layup using carbon fiber sheets. The process for this involves these materials: 3D-printed mold, carbon fiber, peel ply release film, perforated peel ply release film, cotton fabric (bleeder), cotton breather fabric (breather), vacuum bagging film, butyl mastic tape, and epoxy resin.

After carefully cutting all of the films, fabrics, and fibers to the necessary sizes for the mold, the composite fabrication process can begin. Peel ply is the first layer to be put onto the 3D-printed mold using double sided tape to ensure the CFRP will not stick to the mold. Next, two carbon fiber sheets are saturated with epoxy resin using a paint brush. The impregnated carbon fiber sheets are then put on top of the peel ply release film. The perforated peel ply release film is then layered atop the carbon fiber, and the cotton fabric sheet above that. The perforated peel ply has small holes throughout the film which allow the epoxy resin to be pulled out in vacuum and the bleeder is used to soak the excess resin. A layer of peel ply is put on top of the bleeder to prevent the epoxy resin from seeping into any further layers. Breather is laid over the entire layup to provide even pressure across the layup as it cures. Finally, the layup is sealed with a vacuum bag and butyl mastic tape enclosing the layup and the vacuum is connected to the layup to draw out any air and ensure a higher quality composite that is uniformly bonded. This layup process is best depicted in **Figures 6.1.3** and **6.1.4**.

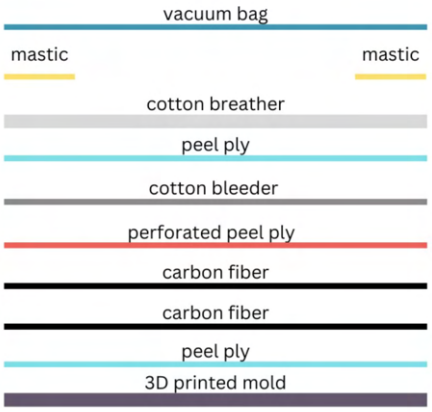

Figure 6.1.2: Composite layup cross section

Figure 6.1.3: Composite layup

Figure 6.1.4: Composite manufacturing during fuselage fabrication

6.1.4 Adhesives

The manufacturing of the aircraft and test vehicle employs four adhesives: cyanoacrylate glue (CA), wood glue, epoxy resin, and Velcro. CA glue is a fast bonding adhesive used for permanent balsa-to-balsa bonds, such as ribs, stringers, and 3D-printed parts. Wood glue provides stronger adhesion for tightly bonded wood interfaces, such as balsa-to-basswood and basswood-to-basswood. Epoxy is used to attach plastic and composite components, forming strong bonds that enhance the structural integrity of composites by reinforcing fibers. Velcro serves as a temporary adhesive for repositionable components, including the fuselage hatch and battery mounts. These adhesives are selected for their specific strengths to ensure optimal performance and reliability.

6.1.5 Machining

By utilizing high power machinery such as conventional mills, it is possible to create accurate, repeatable cuts and holes in durable materials. This process enables the easy production of parts with precise features which are essential for components that require a low tolerance for error, enhancing performance and reducing variability of the aircraft. This was specifically used for manufacturing the steel motor cross mounts.

6.2 Subsystem Manufacturing

6.2.1 Fuselage Manufacturing

The fuselage has a clamshell structure with two hollow carbon fiber halves. Molds of the fuselage were 3D-printed from ABS at the Cornell Rapid Prototyping Lab. The two halves of the fuselage were manufactured separately out of carbon fiber using the molds. A dremel and sand paper were used to correct any imperfections in the shape of the edges of each half from the manufacturing of the carbon fiber. The hollow carbon fiber layups were sealed together with epoxy. Screws were used to fasten the fuselage to the wing, passing through the top of the fuselage and the wing's carbon fiber spar and secured with bolts on the ends. A hatch 6 in x 4.5 in was cut out of the top of the fuselage with a dremel and a hinge was attached to it with screws. Finally, slots were cut in the bottom with a dremel for the test vehicle launch mechanism. The completed fuselage is depicted in **Figure 6.2.1**.

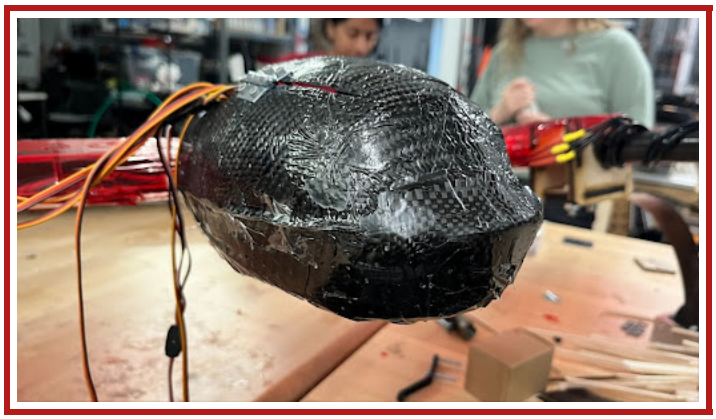

Figure 6.2.1: Completed carbon-fiber fuselage

6.2.2 Wing Manufacturing

The wing structure was made out of balsa wood, hardwood, wood glue, and cyanoacrylate adhesive. The ribs, combs, trailing edge stringers, and servo plates were all laser cut from $\frac{1}{8}$ in balsa wood or hardwood (specifically basswood) depending on whether their main purpose was to bear loads or provide structure. All of the ribs were attached to the hardwood combs with wood glue. The wing spar was used to keep the ribs in alignment along the span. The leading edge was made from $\frac{1}{32}$ in balsa sheets that were soaked in warm water then dried while being molded into the leading edge curve. The rest of the stringers were manually cut with a blade from 1/8 in balsa sheets and attached to the ribs in their notches using CA. The laser cut servo plates were attached to notches on the underside of select ribs using wood glue.

The ailerons were constructed in a similar manner with a front hardwood comb to support the ribs and balsa trailing edge pieces that were attached to the aileron rear comb with wood glue. The wooden wing skeleton structure at this stage in the manufacturing process is shown in **Figure 6.2.2**. Balsa blocks are placed on the inner faces of the rear comb of the wing and the inner faces of the aileron comb to help secure the hinges. Servos were screwed into acrylic plates which were, in turn, screwed into the hardwood servo plates. For both ailerons, manually cut metal control rods were connected from the zeroed servos to the servo horns which sat on the hardwood plate between two ribs of the aileron.

The wing and ailerons were covered with MonoKote and then connected with Robart steel pin hinges through the combs and balsa blocks.

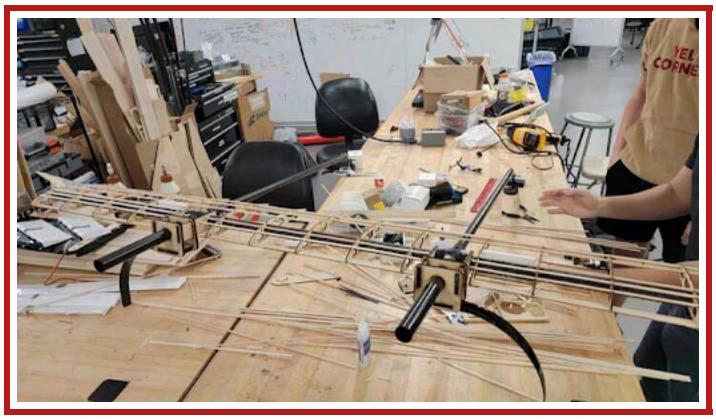

Figure 6.2.2: Wooden wing skeleton structure

6.2.3 Empennage Manufacturing

The tail structure was made out of balsa wood, hardwood, wood glue, and cyanoacrylate adhesive. The ribs, combs, servo plates, and vertical stabilizer spars were laser cut from $\frac{1}{8}$ in balsa wood or basswood depending on whether their main purpose was to bear loads or provide structure. The tail structure was assembled almost identically to the wing. The differences included the exclusion of a carbon fiber spar, the exclusion of the $\frac{1}{32}$ in balsa sheet leading edge for both stabilizers in favor of hardwood stringers, and the exclusive use of balsa trailing edge pieces as the control surfaces extend the entire span of the stabilizers. The vertical stabilizers had a hardwood spar piece while the horizontal stabilizer did not have a spar. The servo assembly for the elevator and rudders was identical to that of the ailerons. Control surfaces and stabilizers were covered with MonoKote and connected with Robart steel pin hinges. The fully MonoKoted aircraft is shown in **Figure 6.2.3**.

6.2.4 Mission Packages Manufacturing

Fuel Tanks The fuel tanks of the aircraft are Gatorade bottles. These payloads will be secured to the wing using pylons manufactured from carbon fiber. A PLA plastic mold was 3D-printed to the shape of the pylons then coated with a layer of a PVA release agent. After the layer has dried, three impregnated carbon fiber sheets were used, instead of two, and placed with the fibers aligned in opposite directions to ensure maximum strength. Once this is done, the excess carbon fiber is cut away using a dremel; velcro straps are glued on to them to fully secure the bottle.

Figure 6.2.3: First iteration of the aircraft

X-1 Vehicle The X-1 vehicle's fuselage was designed in CAD and then sliced along the longitudinal axis into several 0.5 in thick slices. These slices were laser cut into basswood molds and then glued to $\frac{1}{2}$ in thick expanded polystyrene foam (EPS) sheets. These basswood molds allowed for large-scale cuts to be made smoothly and with precision when traced with a hot wire cutter. The slices were then glued together to form the fuselage. The X-1 wing was manufactured using a two inch thick EPS sheet and a basswood mold of the airframe glued against one of the sides of the sheet. The sheet was cut to the required length of the wing and the hot-wire cutter was stretched taut from one side to the other. It was then used to trace the airfoil shape, creating an even airfoil of the required length.

6.3 Manufacturing Milestones

The team employs a manufacturing schedule chart that includes major processes and milestones that must be hit to remain on target. A chart is created for each iteration, and the schedule is refined as the team becomes more familiar with the aircraft design and lessons are learned during each build process. The milestones chart for the competition aircraft is shown in **Figure 6.3.1**. Based on the iteration 1 build, it is expected that the competition aircraft will take approximately three weeks to fabricate. This is planned to occur in March, with a flight test at the end to confirm that all systems are working before departing for the competition. Many of the aircraft components are manufactured simultaneously to speed up the process and make the best use of resources. The last week of any build phase is dedicated to integrating the various pieces and ensuring that they work together properly. Should unforeseen delays occur during the competition aircraft building, there is an extra week after this timeline as a buffer before the aircraft must be shipped to Arizona.

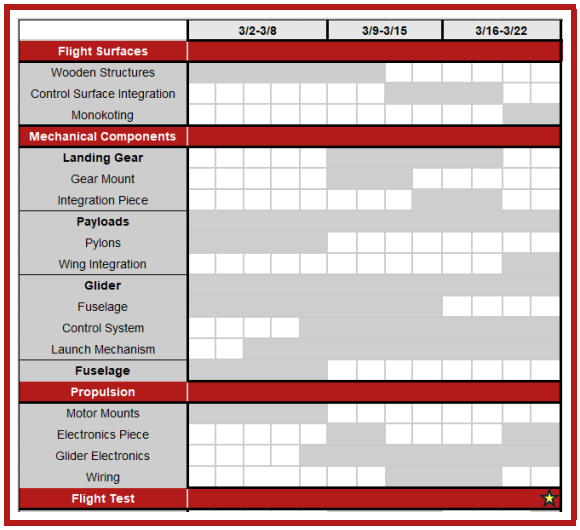

Figure 6.3.1: Manufacturing timeline for the competition aircraft

7 Testing Plan

7.1 Ground Tests

7.1.1 Load and Drop Tests

Wingtip Test The wing was tested to a weight of 24.00 lbs, for a factor of safety of two over the maximum predicted load. During the test, no components failed, and the deflection of the wingtips was negligible. In addition, the center of gravity was found to be near the quarter chord in all three mission configurations. This balance is favorable and indicates that the static margin is as predicted in the theoretical analysis.

Spar Load Test Of the potential carbon fiber spars tested, a 5.30×10^{-3} lb/in square tube with an inner width of 0.79 in and an outer width of 0.89 in was selected due to exhibiting an acceptable tip deflection of less than 0.50 in when fully loaded.

Motor Mount Test The motor mount performed sufficiently, showing no significant deflection or deformation. Loads were relatively evenly distributed through the carbon fiber spar as intended, confirming the design's effectiveness. These results validated the motor mount's structural integrity and compatibility with the propulsion system.

Pylon Load Test The pins successfully supported this load without significant bending. These results indicate that the pins are suitable for carrying the sand-filled bottle during flight, even when subjected to added drag forces. During testing, the carbon fiber/clevis pin integration area was examined for cracks or plastic yielding, and no damage was observed.

Landing Gear Tests The strut was not tested to failure due to safety concerns regarding the fracturing of carbon fiber under extreme loading conditions in the lab, but it was tested beyond the required factor of safety. A load was gradually applied using a load cell, and the deflection was measured at 4.00 lb increments. The maximum load applied was 37.50 lb, causing a vertical deflection of four inches. Since the design gives more than 4 in clearance to the propellers, this amount of deflection is acceptable for the main landing gear. Additionally, it was able to withstand a static load of 1.3 times greater than the required factor of safety and, therefore, passed this loading test.

Fuselage Tests The fuselage was not tested to failure in either test following safety concerns regarding the carbon fiber. In the load test, the fuselage was fit with the expected weight with a factor of safety of 1.5. The loaded fuselage showed no signs of deformation under the weight. In the fuselage drop test, the structure withstood multiple drops with a factor of safety of 1.5 on the force expected in impacts. Visual inspection on the mounted fuselage proved no shearing or deformations. Without any noticeable structural or loadbearing results, the fuselage was declared to pass the load and drop test.

7.1.2 Static Thrust Test

Static thrust testing was conducted using the CM-4515/18 motor to validate expected eCalc values. Several propeller options were used: 14 in x 10 in, 12 in x 12 in, and 12 in x 10 in Using the data-collection capabilities of the new testing rig, thrust-throttle graphs were generated for all tested propeller variations. An example of a propeller on the

testing rig is shown in **Figure 7.1.1**. Data is collected via load cells that transmit a signal to an Arduino which in turn sends it to a script that graphs and analyzes the data.

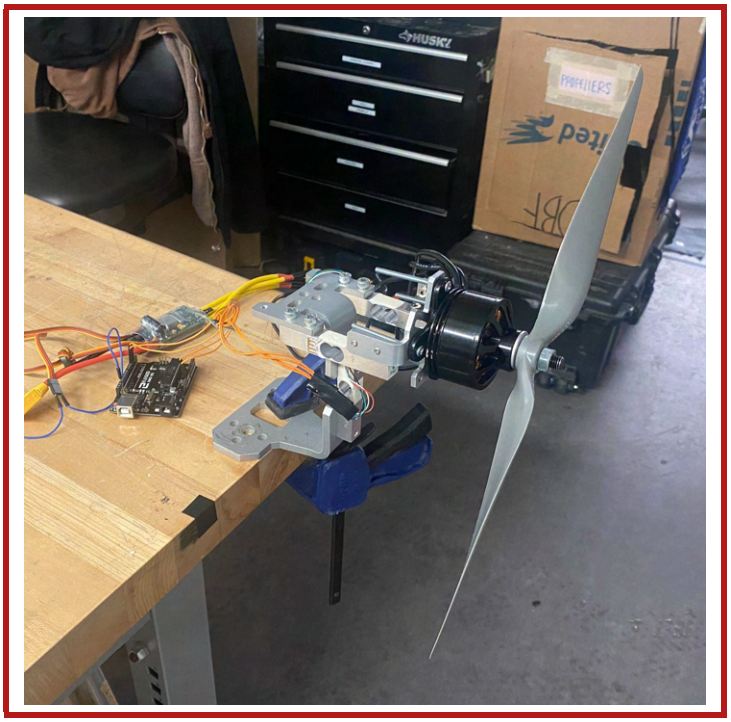

Figure 7.1.1: Static thrust test rig

In order to simulate the behavior of both motors working simultaneously, an L-bracket rig, placed on a freely rotating axle, is modified to account for two motor slots. A bar with similar length to the spacing of the motors on the aircraft is mounted onto the bracket and tests are conducted with the motors working in tandem. The motor mount, motor, and propeller are attached to the upper end of the bar, while the lower end is placed perpendicular to the ground on an electronic scale. The propeller's rotation creates a moment around the L-bar axle, while the lower end of the bar presses down on the scale. Since the two arms of the L bar are equal in length, the mass measured by the scale multiplied by the force of gravity is equal to the thrust generated. For each propeller, the first trial set throttle to 100% to simulate takeoff and the second trial set throttle to 60% to simulate cruising speed.

7.1.3 X-1 Vehicle Tests

Strobe Light Visual Test All observers verified the lights were on and visible from various orientations of the X-1 vehicle. The maximum discernible distance of the strobe lights was identified as roughly 700 ft. Observers also concluded that the most visible light color against the backdrop of the sky was green.

Ground Test of X-1 Vehicle Launch Mechanism The first round of ground testing found that the servo lacked the torque to provide the desired factor of safety. New, stronger servo motors performed successfully in another round of testing, supporting up to 2.5 lb on the end of the launch arm with minimal deflection and no cracks, fractures, or plastic deformation. Testing also confirmed that the mechanism is able to move to the prescribed 10-degree angle of deflection while supporting five times the test vehicle weight.

X-1 Test Flight The X-1 vehicle test flight was carried out to ensure flight stability and generate lift as it descended. The test vehicle is launched off of the roof of Rhodes Hall at Cornell University, approximately 84 ft above the ground. Upon landing, the test vehicle is inspected for any damage.

X-1 Vehicle Elevon Actuation Test The test vehicle elevon actuation was tested to ensure that the deflection was substantial for effective flight control. The elevon deflection was measured at roughly ± 40 degrees from the wing-level position, which is sufficient for the task. Additionally, the test was carried out to ensure that the servo and rod assembly was secure for real flight. The servo showed no signs of overheating and the rods, clamps, and hinges did not show any signs of damage during and after the test.

Autopilot Test After launching the X-1 vehicle from the roof, it was observed to direct itself according to the flight path programmed into the flight controller, successfully countering a slight wind measured at 7.00 mph. The vehicle loitered around its final destination as programmed and touched the ground safely. With all strobe lights and electronics still operational, this concluded a successful test.

7.2 Flight Testing Plan and Data

In order to determine the performance of the aircraft design and to identify potential improvements, a series of flight tests are planned. All flight tests are conducted on the property of the Ithaca Radio Control Society. The team works closely with members of the club to leverage their valuable insights and utilize their years of RC aircraft piloting skills. Flight tests begin with a thorough inspection of the aircraft and a series of ground tests including wingtip balance tests, throttle up tests, and taxi tests to ensure that all systems are safe for flight.

Each iteration of the aircraft culminates with a maiden flight in the M1 configuration to verify its airworthiness. After this, the specific tests conducted depend on the aircraft iteration. Earlier aircraft focus on proof of concept tests including testing M2 and M3. Once the aircraft is shown to be capable of meeting all the mission requirements, the flight testing program switches to data gathering for analysis and optimization. The team developed an in-house Arduino code that attaches to a pitot tube to meausure airspeeds in flight. Using this, data can be obtained about the aircraft performance, including cruise speeds, takeoff speeds, landing speeds, and turning speeds. These data inform predictions on mission performance and score, allowing adjustments to be made, improving the overall aircraft design.

7.3 Flight Test Checklist

The team uses the following pre-flight and pre-takeoff checklists to ensure flight test safety and preparation:

Pre-Flight Checklist

Last Updated: Feb, 2025

Flight Test Date:_____

Task	✓	Remarks
Electrical Power Sources		
Verify Main Propulsion Battery at full charge		
Verify Receiver Battery at full charge		
Verify Transmitter Battery at full charge		
Aeronautics		
Verify wings are well secured to the fuselage		
Identify location of center of gravity		
Wingtip test		
Actuation		
Zero servos		
Correct servo connections to receiver, battery and ESC		
Ensure servos are securely fastened		
Verify control surfaces have enough deflection		
Propulsion		
Ensure correct propeller is mounted		
Ensure propeller is securely fastened		
Ensure we are using a Right (not Left) propeller		
Miscellaneous Tests		
Landing Gear/Roll Test		
PropulsionMountStructuralTest		
Transmitter Range Test		
Record total prop weight and total plane weight		
Flight Contingency Case Manifest		
LiPoProtectiveBag		
ElectricalTape,DuctTape,HingeTape		
Scissors,XactoKnives(2) HandDrillandDrillBits		
CAGlue(2,InstantandGapFilling)andExtraTips		
Balsasheet(⅛,1/16),balsastringers		
ExtraTransmitter,Receiver,ESC Thermal Blanket for		
Cold Weather 2xsetsofAllenKeys BoltsandNuts		
Logistics		
File for FAA approval		

Pre-TakeoffChecklist

Task	✓	Remarks
50% Throttle, Throttle Closed, Full Up Elevator, Full Right Rudder, Full Right Aileron		
Radio Failsafe set, Arming plug in possession Propeller rotating in correct direction		

Signature:_____

8 Performance Results

8.1 Subsystem Test Results

8.1.1 Load and Drop Test Results

Wingtip Test The wing was tested to a weight of 24.00 lbs, for a factor of safety of two over the maximum predicted load. During the test, no components failed, and the deflection of the wingtips was negligible. In addition, the center of gravity was found to be near the quarter chord in all three mission configurations. This balance is favorable and indicates that the static margin is as predicted in the theoretical analysis.

Spar Load Test Of the potential carbon fiber spars tested, a 5.30 x 10^{-3} lb/in square tube with an inner width of 0.79 in and an outer width of 0.89 in was selected due to exhibiting an acceptable tip deflection of less than 0.50 in when fully loaded.

Motor Mount Test The motor mount performed sufficiently, showing no significant deflection or deformation. Loads were relatively evenly distributed through the carbon fiber spar as intended, confirming the design's effectiveness. These results validated the motor mount's structural integrity and compatibility with the propulsion system.

Pylon Load Test Demonstrated in **Figure 8.1.1**. The pins successfully supported this load without significant bending. These results indicate that the pins are suitable for carrying the sand-filled bottle during flight, even when subjected to added drag forces. During testing, the carbon fiber/clevis pin integration area was examined for cracks or plastic yielding, and no damage was observed.

Figure 8.1.1: Pylon testing apparatus

Landing Gear Tests The strut was not tested to failure due to safety concerns regarding the fracturing of carbon fiber under extreme loading conditions in the lab, but it was tested beyond the required factor of safety. A load was gradually applied using a load cell, and the deflection was measured at 4 lb increments. The maximum load applied was 37.5 lb, causing a vertical deflection of four inches as shown in **Figure 8.1.2**. Since the design gives more than 4 in clearance to the propellers, this amount of deflection is acceptable for the main landing gear. Additionally, it was able to withstand a static load of 1.3 times greater than the required factor of safety and, therefore, passed this loading test.

Figure 8.1.2: Landing gear testing apparatus

Fuselage Tests The fuselage was not tested to failure in either test following safety concerns regarding the carbon fiber. In the load test, the fuselage was fit with the expected weight with a factor of safety of 1.5. The loaded fuselage showed no signs of deformation under the weight. In the fuselage drop test, the structure withstood multiple drops with a factor of safety of 1.5 on the force expected in impacts. Visual inspection on the mounted fuselage proved no shearing or deformations. Without any noticeable structural or load bearing results, the fuselage was declared to pass the load and drop test.

8.1.2 Static Thrust Test Results

Static thrust testing was conducted using the CM-4515/18 motor to validate expected eCalc values. Several propeller options were used: 14 in x 10 in, 12 in x 12 in, and 12 in x 10 in. Using the data-collection capabilities of the new testing rig, thrust-throttle graphs were generated for all tested propeller variations. Initial tests, illustrated in **Figure 8.1.3**, suggested the propulsion configuration was severely limited, missing expected thrust targets. Further investigation identified improper calibration of the ESCs as the leading cause. This problem was solved in later tests, leading to the successful achievement of expected mission targets as shown in **Table 8.1.1**. Following the testing, the 14 in x 10 in propeller was selected for its superior flight time and thrust.

Propellers	Max Thrust (lbf)	Flight Time (minutes)
15 in x 9 in	13.28	3.4
14 in x 10 in	12.45	4.9
12 in x 12 in	12.02	6.2

Table 8.1.1: Propeller Specifications

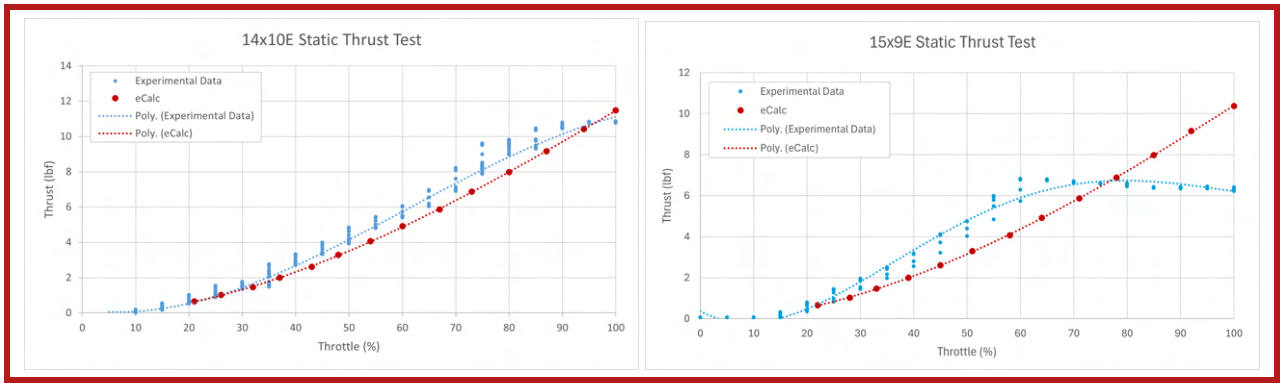

Figure 8.1.3: 14 x 10E and 15 x 9E Static Thrust Test Results.

8.1.3 X-1 Test Vehicle Test Results

Strobe Light Visual Test All observers verified the lights were on and visible from various orientations of the X-1 vehicle. The maximum discernible distance of the strobe lights was identified as roughly 700 ft. Observers also concluded that the most visible light color against the backdrop of the sky was green.

Ground Test of X-1 Vehicle Launch Mechanism Results The first round of ground testing found that the servo lacked the torque to provide the desired factor of safety. New, stronger servo motors performed successfully in another round of testing, supporting up to 2.5 lb on the end of the launch arm with minimal deflection and no cracks, fractures, or plastic deformation. Testing also confirmed that the mechanism is able to move to the prescribed 10-degree angle of deflection while supporting five times the test vehicle weight.

X-1 Vehicle Elevon Actuation Test The test vehicle elevon actuation was tested to ensure that the deflection was substantial for effective flight control. The elevon deflection was measured at roughly ± 40 degrees from the wing-

level position, which is sufficient for the task. Additionally, the test was carried out to ensure that the servo and rod assembly was secure for real flight. The servo showed no signs of overheating and the rods, clamps, and hinges did not show any signs of damage during and after the test.

Autopilot Test Results After launching the X-1 vehicle from the roof, it was observed to direct itself according to the flight path programmed into the flight controller, successfully countering a slight wind measured at 7.00 mph. The vehicle loitered around its final destination as programmed and touched the ground safely. With all strobe lights and electronics still operational, this concluded a successful test.

8.2 Aircraft Performance and Improvements

8.2.1 Field Testing

The first flight test took place on December 12, 2024, with the main goal to get a performance baseline and seek improvements for the next iterations of the aircraft. A pre-flight wingtip test showed that the aircraft was longitudinally and laterally stable. During the flight test preparations, the team observed issues with the control surfaces, specifically the elevator. Due to an insufficient number of hinges near the middle, it failed to deflect correctly and began to bend. Otherwise, all other control surfaces were verified to be acceptable for flight. At this point, it was deemed the aircraft was not feasible for flight as the elevators needed to be able to fully deflect for full control of the aircraft pitch. The gyroscope was also tested at this time by tilting the aircraft in different axes and the control surfaces deflected in the appropriate directions, so the gyroscope was verified to be working properly. In order to gain insight into the aircraft, a taxi test was performed in lieu of the flight attempt. During the taxi, the aircraft moved stably and was controllable with the rudders, validating the absence of ground steering. At the end of taxi, the landing gear integration piece sheared off after hitting a bump, and the ESC short-circuited.

Initial performance expectations were not met by Iteration 1, which was to complete 3 laps under M1 conditions. The tests revealed issues manufacturing quality of the elevator, landing gear integration, and the propeller-motor integration. There were also significant complications with the wiring of the electronics.

Solutions were suggested and implemented after subsystem tests occurred and were verified to be acceptable for the aircraft. Specifically, the elevator was redesigned to have more hinges connecting the elevator to the horizontal stabilizer. It was then tested and shown to have the appropriate amount of deflection with different pitch control. The motor mounts were adapted to ensure the motor and propellers remained securely joined to the spar to minimize the risk of detachment. The issues in iteration 1 have been addressed and initial subsystem tests on iteration 2 are promising.

Figure 8.2.1: Flight test preparation

References

[1] AIAA Foundation. *2024-25 Design, Build, Fly Rules*. AIAA. Aug. 2024.

[2] ANSYS, Inc. *ANSYS® Academic Research Mechanical 2021*. Available online at https://www.ansys.com/. 2021.

[3] ArduPilot Development Team. *ArduPlane, ArduCopter, ArduRover Source*. Available online at https://github.com/ArduPilot/ardupilot. 2017.

[4] *MATLAB, version 23.0.24 (R2023b)*. The MathWorks Inc. Natick, Massachusetts, 2024.

[5] Markus Mueller. *propCalc - Propeller Calculator*. Available online at https://www.ecalc.ch/motorcalc.php. Apr. 2017.

[6] S. Ravikanth et al. "A Effect of Elevator Deflection on Lift Coefficient Increment". In: *International Journal of Modern Engineering Research (IJMER)* (2015). Available online at https://www.ijmer.com/papers/Vol5_Issue6/Version-1/B0506_01-0925.pdf.

[7] Daniel Raymer. "Airfoil and Geometry Selection". In: *Aircraft Design: A Conceptual Approach, Second edition*. Washington, D.C., 1992, p. 56.

[8] S. P. Setyo Hariyadi, Sutardi, and Wawan Aries Widodo. "Numerical Study of Aerodynamic Analysis on Wing Airfoil NACA 43018 with the Addition of Forward and Rearward Wingtip Fence". In: (2016). Retrieved from https://pubs.aip.org/aip/acp/article/1778/1/030011/779923/Numerical-study-of-aerodynamic-analysis-on-wing.

[9] Gloria Stenfelt and Ult. Ringertz. *Lateral Stability and Control of a Tailless Aircraft Configuration*. Retrieved from https://www.researchgate.net/publication/245431197_Engineering_Notes_Lateral_Stability_and_Control_of_a_Tailless_Aircraft_Configuration. 2008.

[10] Dassault Systems. *Solidworks*. Available online at http://www.solidworks.com/. 2024.

[11] G. Van Rossum and F. L. Drake. *Python 3 Reference Manual*. Scotts Valley, CA: CreateSpace, 2009.

[12] L.L.M. Veldhuis. "Review of Propeller-Wing Aerodynamic Interference". In: *24th International Congress of the Aeronautical Sciences*. Retrieved from https://www.sciencedirect.com/science/article/pii/S1369886901000. 2004.

[13] *XFLR5*. Available online at http://www.xflr5.tech/xflr5.html. 2023.

[14] Y. Zhang, H. Chen, and Y. Zhang. "Wing Optimization of Propeller Aircraft Based on Actuator Disc Method". In: *Chinese Journal of Aeronautics* 34.5 (2021). Retrieved from https://www.sciencedirect.com/science/article/pii/S1369886901000, pp. 65–78. DOI: 10.1016/j.cja.2020.12.032.